

Sensitivity of Climate Drift to Atmospheric Physical Parameterizations in a Coupled Ocean–Atmosphere General Circulation Model

LAURENT TERRAY

Climate Modelling and Global Change Project, CERFACS, Toulouse, France

(Manuscript received 5 May 1997, in final form 20 August 1997)

ABSTRACT

Sensitivity of climate drift to selected convection and cloudiness parameters is investigated with a coupled ocean–atmosphere general circulation model. The dependence of the coupled model climatology upon parameterizations of convective entrainment and stratocumulus cloud cover is studied. The methodology relies upon short uncoupled (1 yr) and coupled (3 yr) simulations. The coupled model climatology is very sensitive to both parameterizations. For instance, the air–sea interface mean state can be too warm or too cold depending on the profile of the convective entrainment rate. Enhanced entrainment at lower levels breaks the symmetry of the tropical precipitation pattern observed in both forced and coupled control simulations. Furthermore, the zonal wind stress strength and related thermocline slope around 150°W are shown to be crucial in determining the warm pool–cold tongue structure in the tropical Pacific. The model sensitivity is found to be the result of complex feedbacks between convection, cloud, and boundary layer processes, sea surface temperature (SST), and large-scale ocean–atmosphere dynamics.

1. Introduction

Ocean–atmosphere interactions play a crucial role in understanding climate variability on a broad range of spatial and timescales. Coupled ocean–atmosphere general circulation models (CGCMs) are the most comprehensive and, potentially, the most appropriate tools to simulate and understand the global climate and its present-day fluctuations such as the El Niño–Southern Oscillation phenomenon. The development and validation of CGCMs are currently carried on in a number of institutions worldwide. Major unresolved issues in coupled modeling involve model initialization, coupling strategy, and climate drift (Meehl 1995). The latter not only affects the climate mean state but also its variability. Furthermore, it is present in both global and limited domain coupled models (Neelin et al. 1992; Meehl 1990). If one wants to avoid the questionable use of flux correction (Neelin and Dijkstra 1995), the understanding and reduction of climate drift are then one of the highest priorities in climate research.

Climate drift can be defined as the departure of the CGCM climatology from the observed one as well as from the climate simulated by the GCMs in uncoupled mode (Neelin et al. 1994). In the case of high-resolution tropical GCMs, it usually appears as a fast adjustment

(over a period of few months) toward an equilibrium state that can significantly differ from the observed one. Analysis of the initial adjustment phase and of the error at equilibrium are both necessary to understand the model biases.

In this work, the climate drift issue is addressed by means of sensitivity experiments with a CGCM to the parameterizations of selected atmospheric processes. A recent intercomparison of CGCMs (Meechoso et al. 1995) has uncovered some of the most widespread systematic errors present in tropical climate simulations: a warm SST bias over the southeast Pacific and in a narrow tongue along 10°S. These deficiencies are associated with either a double intertropical convergence zone (ITCZ) or an ITCZ that migrates across the equator with the seasons. The CGCMs are therefore unable to maintain the asymmetry of the observed system. Another bias is the difficulty to simulate the seasonal cycle of equatorial SST in the eastern Pacific. Among the 11 CGCMs, only 4 were able to capture the annual harmonic quite realistically. Furthermore, even in these models, the cold tongue appears prematurely and its development is too rapid. Westward propagation of SST anomalies is not always well simulated indicating sharp transition in the trade wind regime (Meechoso et al. 1995; Terray et al. 1995). The CERFACS model referenced in Meechoso et al. (1995) is identical to the one used in this study.

Why is the ITCZ located north of the equator? The question is still under intense debate and no definite answer has been given (Mitchell and Wallace 1992;

Corresponding author address: Dr. Laurent Terray, Climate Modelling and Global Change Project, CERFACS, 42 avenue Gustave Coriolis, 31057 Toulouse Cedex, France.
E-mail: terray@cerfacs.fr

Giese and Carton 1994; Philander et al. 1996). Nevertheless, the failure for CGCMs to maintain the asymmetric meridional structure in the eastern Pacific strongly suggests the crucial role of coupled feedbacks on the link between deep atmospheric convection and SST. Some of the mechanisms commonly invoked are stratocumulus (SC) cloud effects (Klein and Hartmann 1993; Ma et al. 1996; Philander et al. 1996), the evaporation–wind feedback mechanism associated with equatorial upwelling and oceanic mixing (Xie 1994; Xie and Philander 1994), and coastal upwelling. Warm modeled SSTs off the west coast of subtropical continents are often associated with the poor representation of boundary layer SC clouds in these regions. Observed thin layers of marine stratiform decks below the inversion in the planetary boundary layer (PBL) are commonly known to form in response to strong subsidence generated by the subtropical high over a relatively cold upwelling ocean. In northern winter, the simulated SSTs south of the equator are warm enough so they can initiate deep atmospheric convection and displace the ITCZ southward. Weak coastal upwelling due to a weak onshore wind component can also be responsible for the insufficient SST cooling along the South American coast. Once a convergence zone is established south of the equator, it may persist due to feedback mechanisms which probably vary with models. For instance, the CERFACS model uses a convection scheme of the mass flux type, which is known to dry out the lower atmosphere by the effect of induced subsidence. This, in turn, tends to increase surface evaporation, which maintains the convection through a positive feedback loop.

Simple and intermediate models have been used to clearly identify and quantify coupled feedback processes, in particular those involving the wind stress (Dijkstra and Neelin 1995). Nevertheless, sensitivity studies with CGCMs are the expensive albeit necessary way to include the whole set and complexity of physical mechanisms needed for the detailed understanding of air–sea interaction. Section 2 describes the atmospheric and oceanic components of the coupled model. The standard cloudiness and convection parameterizations are thoroughly detailed as well as the changes made for this study. Section 3 presents the results from the sensitivity experiments conducted, both uncoupled and coupled ones. The substantial impact of the parameterization changes on both aspects of climate drift are analyzed in terms of coupled physical processes in section 4. Section 5 gives a summary and directions for future work.

2. The ARPEGE–OASIS–OPA coupled model

a. The ARPEGE model

The atmospheric GCM (AGCM) used in the present study is derived from the ARPEGE/IFS forecast model and is described by Déqué et al. (1994). The present

version uses a spectral T42 triangular horizontal truncation equivalent to a Gaussian grid with a resolution of about $2.8^\circ \text{ lat} \times 2.8^\circ \text{ long}$. The model is vertically discretized with 30 levels extending from the ground up to about 70 km using a progressive vertical hybrid coordinate and has good resolution in the stratosphere. The semi-implicit integration scheme allows for a 15-min time step. The model has a comprehensive package of physical parameterizations. The radiation scheme is a modified and simplified version of the Ritter and Geleyn (1992) scheme. It uses a two-stream approximation of the radiative transfer equation both in the solar and infrared parts of the spectrum (Geleyn and Hollingsworth 1979). The radiation code is called every time step thereby allowing accurate interactions with cloud cover and the diurnal cycle. Parameterizations of boundary layer and turbulence are based on vertical-exchange coefficients computed as functions of the local Richardson number according to the method of Louis et al. (1982). A representation of shallow convection is taken into account through a simple modification of the Richardson number by consideration of the gradient of specific humidity deficit in the vertical stability computation (Geleyn 1987). This is equivalent to a reduction of the Richardson number (increased instability) when the specific humidity gradient exceeds that of a saturated atmosphere. The performed sensitivity experiments concern the treatment of cloudiness and convection, which are detailed in the next paragraphs.

1) CLOUDINESS PARAMETERIZATION

The partial cloud cover is a combination of stratiform and convective cloudiness. The stratiform cloudiness n_{sl} at level l is calculated according to

$$n_{sl} = \min \left[n_{s\max}, \left(\frac{q/q_{\text{sat}} - r_{\text{cl}}^l}{1 - r_{\text{cl}}^l} \right)^2 i_s \right], \quad (1)$$

where $n_{s\max}$ is the maximum cloudiness in a given layer (here 0.6), q and q_{sat} are the specific humidity and its value at saturation, r_{cl}^l is a critical humidity profile, and i_s is the stability index of the layer ($i_s = 0$ if $s_l \leq s_{\text{surf}}$, $i_s = 1$ otherwise). The critical humidity profile is specified as

$$r_{\text{cl}}^l = 1 - \beta_1(\sigma)^{m_1} [1 - (\sigma)^{m_2}] [1 + \beta_2^{0.5}(\sigma - 0.5)], \quad (2)$$

where σ is the ratio of pressure over surface pressure and β_1 , β_2 , m_1 , and m_2 are empirical parameters. These parameters are adjusted to give a balanced radiative budget at the top of the atmosphere on an annual mean basis. The calibration is carried out in order to get a planetary albedo of 0.30.

The total convective cloudiness is given by

$$n_c = \begin{cases} \min(0.5, \beta_3 F_{\text{cp}}) & \text{if the convection is active} \\ 0 & \text{otherwise,} \end{cases} \quad (3)$$

where F_{cp} is the convective precipitation at the previous

time step and β_3 an empirical coefficient. The total convective cloudiness is equally distributed among the active layers with the random overlap hypothesis. The cloud cover at each level is calculated by combining the stratiform (n_{sl}) and convective (n_{cl}) fractions with random overlap:

$$n_c = n_{sl} + (1 - n_{sl})n_{cl}. \quad (4)$$

To improve the representation of the subtropical SC fields, another cloud parameterization, based on Slingo (1987), was introduced in the model. These marine clouds are strongly linked to the PBL and are generally associated with low-level inversions in temperature and humidity. As they are often vertically subgrid scale, they may not be represented accurately by the average relative humidity through a model layer. The proposed parameterization requires a positive vertical velocity (subsidence) and a dry static energy gradient ($\partial s/\partial\Phi$) greater than a critical value [$(\partial s/\partial\Phi)_{crit}$], which defines low-level atmospheric stability. Furthermore, an additional dependence on relative humidity is accounted for, to prevent cloud formation under dry inversions such as those over the winter pole. A critical relative humidity profile is defined:

$$r_{cl}^2 = \min\left\{1 - \epsilon, \max\left[0, 1 - 4H_2 \frac{(1 - \sigma)(\sigma - \sigma_i)}{(1 - \sigma_i)^2}\right]\right\}, \quad (5)$$

where H_2 is an empirical coefficient equal to 0.4 and σ_i the top of the cloudy layer (here 0.8). So the critical humidity is $1 - \epsilon$ both at the surface and 800 hPa and goes through a minimum (0.6) at 900 hPa. Note that there are no clouds above the σ_i level. The SC cloudiness is then given by

$$n_{scl} = \delta_{\omega>0} \min\left\{1 - \epsilon, K_{sc} \max\left[0, \frac{\partial s}{\partial\Phi} - \left(\frac{\partial s}{\partial\Phi}\right)_{crit}\right]\right\} \times \max\left(0, \frac{q/q_{sat} - r_{cl}^2}{1 - r_{cl}^2}\right), \quad (6)$$

where K_{sc} is an empirical coefficient. The empirical coefficients were tuned to ensure the simulation of stratus decks in the anticyclonic regions of the subtropical oceans.

This choice for the stratus parameterization contrasts with previous studies (Ma et al. 1996; Philander et al. 1996), which used either a constant value or an empirical formula applied as a flux correction for the evaluation of the related cloudiness. The described parameterization fully interacts with the atmospheric physics package, allowing a more complete description of cloud–radiation interaction.

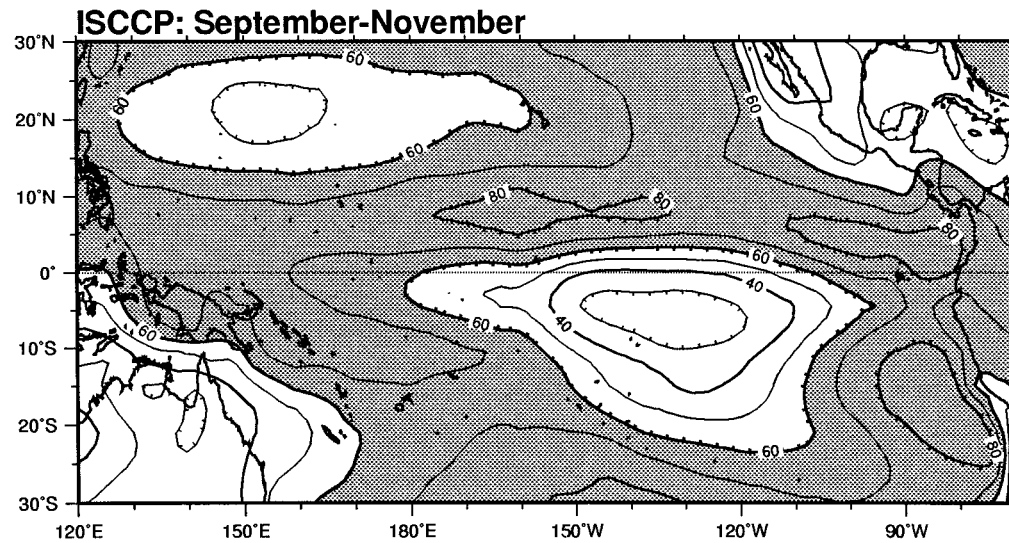
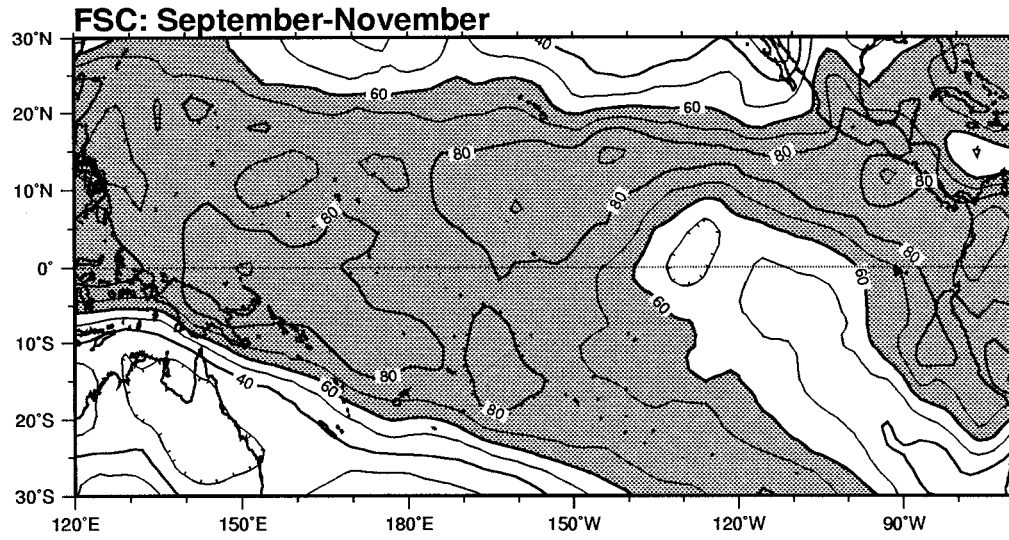
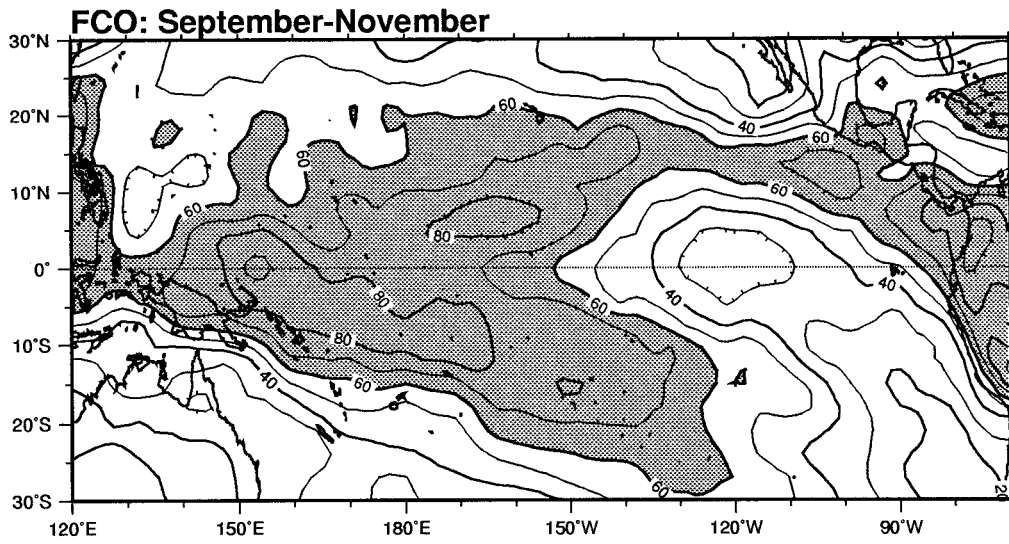
2) CONVECTION PARAMETERIZATION

The effects of cumulus convection on the heat and water large-scale budget is represented by a mass flux scheme with detrainment as proposed by Bougeault (1985). The cloud profile is determined by a moist adiabat incorporating the entrainment of environmental air with a given profile for the entrainment rate (ER). In the standard version, the ER is constant with height within the convective column and its value is $5 \times 10^{-5} \text{ m}^{-1}$. This scheme includes prediction of the convective mass flux inside the cloud and a detrainment term simply proportional to the excess of cloud temperature and moisture over the environmental values. The detrainment coefficient is obtained from conservation of the moist static energy of the convective column. The vertical profile of mass flux is assumed to be proportional to the square root of the moist static energy excess of the cloud. The coefficient of proportionality is determined by a Kuo-type hypothesis relating it to large-scale moisture convergence and turbulent water transport at the cloud base. The evaporation of convective precipitations below the cloud base is not taken into account. As previously noted, this scheme leads to an excessive drying of the lower-atmospheric layers. Furthermore, the standard mass flux scheme is allowed to operate at all places where moisture convergence takes place, caused either by surface evaporation or the atmospheric circulation. Convection is then active over the major part of the tropical oceans, resulting in widespread weak precipitation and poorly defined convergence zones.

A variation with height of the ER, similar to the one used by Gregory and Rowntree (1990), has been implemented in order to reduce this bias (Geleyn et al. 1994). The ER is maximum at the bottom of the convective column, and relaxes exponentially toward the standard value as one goes up the cloud. The maximum value is taken equal to $4 \times 10^{-4} \text{ m}^{-1}$. The varying entrainment assumption is also based on physical and observational evidence, which supports an inverse-cloud radius entrainment law (Simpson 1971). The intuitive idea is to reduce the upward convective mass flux in order to increase specific humidity at low levels.

b. The OPA model

The oceanic component of the CGCM is based on the OPA model developed at the Laboratoire d'Océanographie Dynamique et de Climatologie (Delecluse et al. 1993) and adapted to the tropical Pacific by Dandin (1993). It is a finite-difference model based on the primitive equations with the Boussinesq approximation. The model uses the rigid-lid assumption to eliminate surface gravity waves. The parameterization of vertical mixing by turbulence is a 1.5-order turbulent kinetic energy (TKE) closure scheme (Blanke and Delecluse 1993). Horizontal diffusion is harmonic with



eddy coefficients of $10^3 \text{ m}^2 \text{ s}^{-1}$ for tracers and momentum. Penetrative solar radiation is allowed to penetrate surface layers. The model domain covers the Pacific Ocean from 120°E to 70°W and 40°S to 48°N . The horizontal resolution is 0.75° long and between 0.33° and 1.5° lat (with the highest resolution near the equator). Twenty-eight vertical levels are chosen with 17 levels in the upper 400 m. A gridded bathymetric dataset of $5' \times 5'$ (ETOP5 1986) resolution has been interpolated onto the model mesh. The abyssal trenches have been cut off at 4950 m and islands submerged at 700 m. The temperature and salinity fields are constrained to climatological values (Levitus 1982) with a restoring coefficient varying with depth as proposed by Sarmiento and Bryan (1982). The salinity restoring coefficient decreases exponentially from 4 day^{-1} at the surface to 2 yr^{-1} at the ocean bottom. The temperature restoring coefficient increases from 0 at the sea surface to 13 day^{-1} at 150 m and then decreases to 2 yr^{-1} at the bottom. This vertical profile is modified according to latitude and distance from the coast (Dandin 1993). It is multiplied by a function set to zero at the equator and increasing smoothly in latitude. This technique keeps the equatorial features free from an imposed climatology and Fujio and Imasato (1991) have shown that it prevents inconsistencies due to the geostrophic adjustment. Furthermore this avoids the sharp transition between the free and restored regions. The relaxation vanishes within 1000 km of the coast. This allows the swift western boundary currents to adjust freely in regions where ageostrophic terms become important.

c. The coupling scheme: OASIS

The OASIS coupling software (Terray 1995) has been used to carry out all the experiments in coupled mode. The GCMs are coupled synchronously by exchanging information once per day, averaging out the diurnal cycle. SST and sea ice extent (SIE) are given to the AGCM and surface fluxes of heat, momentum, and freshwater to the OGCM. SST outside the Pacific domain and the SIE field are prescribed from an observed monthly climatology from the Center for Ocean–Land–Atmosphere–Climate Analysis Center dataset over the 1979–88 period (Reynolds 1988). Modeled SSTs at the northern, southern, and western boundary are modified to smooth out the transition between prescribed and simulated SST. The higher-resolution SST is spatially averaged before being transferred to the AGCM. The surface fluxes are interpolated onto the OGCM grid using bicubic interpolation and without flux correction. However, in order to be consistent with the SST smoothing,

an additional term has been included in the total heat flux response of the atmosphere to a computed SST_{oce} . The heat flux received by the ocean model is then given by

$$Q_{\text{oce}} = Q_{\text{atm}} + K_c(\text{SST}_{\text{oce}} - \text{SST}_{\text{clim}}), \quad (7)$$

where Q_{atm} is the total heat flux computed by the atmospheric model (defined as the sum of the shortwave, longwave, latent, and sensible surface heat fluxes) and SST_{clim} the prescribed climatological SST. The coefficient K_c is zero inside the 25°S – 25°N latitude band and increases linearly to reach $-40 \text{ W m}^{-2} \text{ K}^{-1}$ at the ocean grid boundaries. The same technique also applies for the western boundary, but over a 10° long range within the model grid. The atmospheric uncoupled simulations have been carried out for a 14-month period to account for initial atmospheric transients. The surface boundary conditions are given by climatological SSTs. The coupled experiments run for a period of 3 yr.

3. Sensitivity experiments

In this section, we study the sensitivity of the CGCM to the parameterizations of SC clouds and convective ER. The strategy relies on comparison of the control and perturbed simulations, where the parameterizations are modified one by one. The AGCM used in the control experiments does not use the parameterization of SC clouds, and the ER is constant with height within the convective column. The OGCM is exactly the same in all the numerical experiments performed in this work. The Comprehensive Ocean–Atmosphere Data Set data as analyzed by Oberhuber (1988) are used as a reference (OBE) to which the model output can be compared.

We shall name these different sensitivity experiments using a combination of letters that encapsulates information on the nature of the simulation (forced or coupled) and the parameterizations used. The first letter in the experiment name indicates its nature (F for forced and C for coupled); the following two letters give the added or modified parameterization (CO for the control, SC for stratocumulus clouds, and ER for convective entrainment rate). So, for instance, the uncoupled and coupled control experiments are named FCO and CCO, respectively. The initial atmospheric state comes from an Atmospheric Model Intercomparison Project (AMIP) experiment where the AGCM was forced by observed SSTs over the 1979–88 period. The initial oceanic state comes from an oceanic simulation where the OGCM was forced by the atmospheric fluxes generated by the AMIP simulation. The initial restart date for the coupled simulations corresponds to 1 January 1986. All the maps

←

FIG. 1. Geographical distributions of the monthly averaged total cloud amount for the SON season simulated with (a) FCO, (b) FSC, and derived from the ISCCP dataset (c) between 30°N and 30°S . Units are in percent and contour intervals are every 10%. Shading corresponds to values greater than 60%.

shown in the next two sections are averages over 1 and 2 (the last ones) yr for the forced and coupled simulations, respectively. Although 3 yr is a short period, it is long enough to assess whether the simulated climate drifts differ drastically from each other. Furthermore, the above coupled system is designed to study the tropical atmosphere–upper ocean system where the ocean surface and mixed layer adjust with short timescales to changes in the forcing fields. For instance, it takes about 1 yr to establish all the upper-ocean currents when one initializes a tropical ocean model at rest with climatological temperature and salinity and drives it with realistic wind stress and heat fluxes.

a. Uncoupled experiments: FCO, FSC, and FER

To begin, we inspect maps of cloudiness, water vapor, and relative humidity to check the effect induced by changes in the parameterizations of SC clouds and convective entrainment rate, respectively. Figure 1 shows total nebulosity during the September–November (SON) period for FCO, FSC, and the International Satellite Cloud Cover Project (ISCCP) dataset (Rossow and Schiffer 1991). The SON period is the peak stratus cloud amount for the Peruvian region (Klein and Hartmann 1993). A much improved representation of nebulosity is obtained in the FSC simulation, due to the additional clouds over the subtropical regions. Consequently, the solar heat flux FSC values are strongly reduced (up to 80 W m^{-2}) west of the Peruvian and, to a lesser extent, Californian coasts (not shown). Furthermore, the choice of parameters for the SC parameterization results in increased cloudiness over the whole domain with too large values over the equatorial western and central Pacific.

The impact of the convective entrainment change on the zonal moisture and cloudiness distributions for July can be seen in Fig. 2. The lower-tropospheric specific humidity strongly increases in the northern Tropics as well as in the extratropical cyclonic storms regions. The tropical increase extends from the surface to 500 hPa with a maximum around 800 hPa within the ITCZ. Secondary maxima are observed at midlatitudes associated with a smaller vertical extent.

The relative humidity difference field (Fig. 2b) shows a complex pattern with a dipole structure for the maxima in the northern Tropics, linked with a middle-tropospheric negative minimum in the southern Tropics. The peak increase is depicted in the southern midlatitudes with strong vertical extent. The maxima regions are characterized by strong vertical motions (net rising motion). The associated adiabatic cooling induces saturation

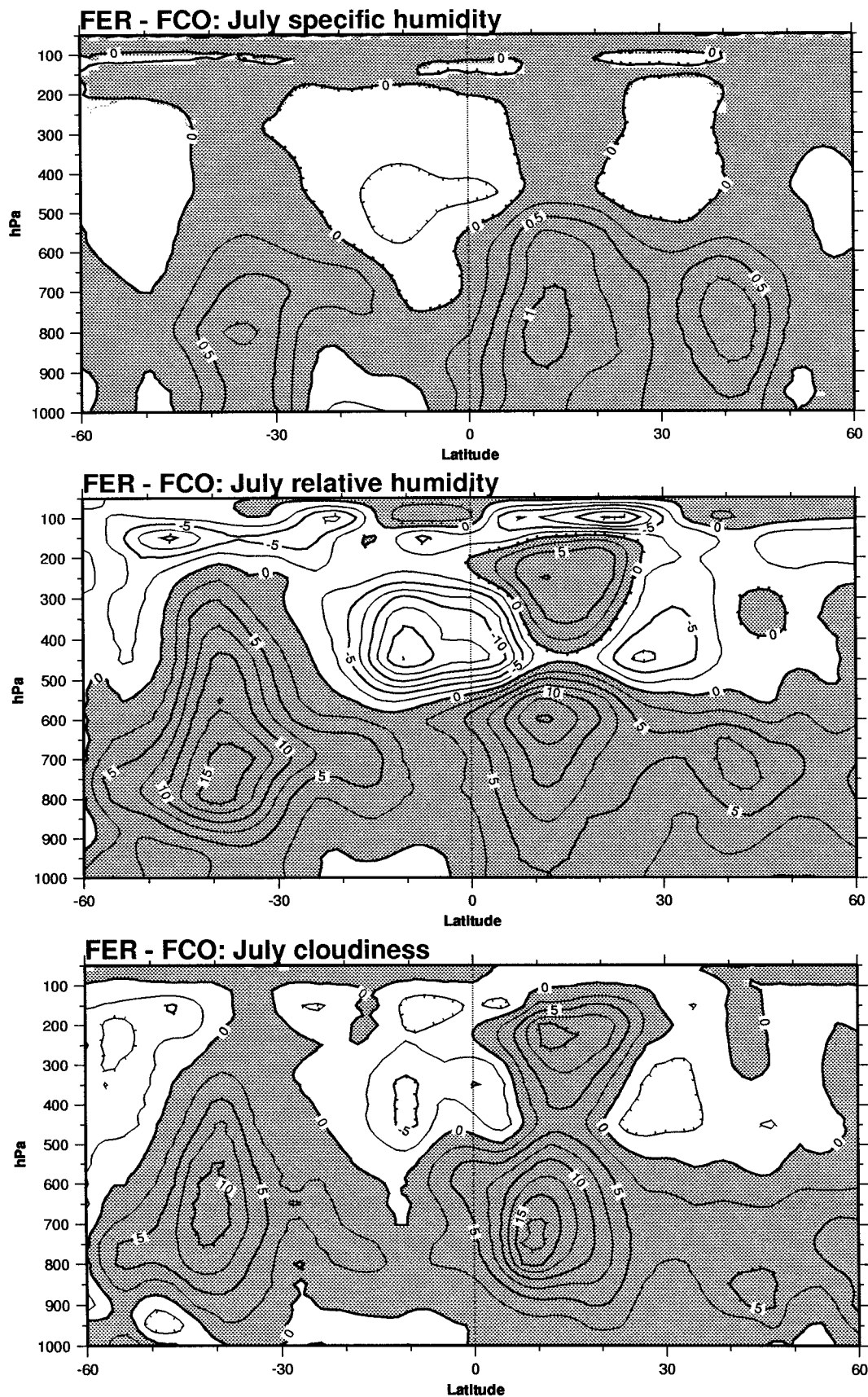
and acts to increase relative humidity through its effect on saturation vapor pressure. Thus a detailed analysis of this pattern requires the knowledge of the differential adiabatic cooling between the two experiments (this will be discussed further below). The cloud cover difference (Fig. 2c) shows very similar patterns due to its quadratic dependency in relative humidity for the stratiform part (1).

Changes in the simulated surface fluxes are now investigated focusing on those that can potentially impact the behavior of the coupled system the most. The total heat flux annual mean is displayed in Fig. 3 for the FCO, FSC, and FER simulations as well as for the OBE data. The FSC and FER values are smaller than the FCO ones and closer to the OBE data in the equatorial eastern Pacific. The decrease in solar heat flux due to increased cloudiness is responsible for the diminished total heat flux (Fig. 1). Over the equatorial warm pool region, the FSC and FER values are weakly positive and negative, respectively. Again the reduction in solar heating plays the main role with an increase of the latent heat flux in the FER case (not shown). Similar effect is found at higher latitudes (between 10° and 30°) in the central and western Pacific. The reduced solar radiation leads to negative total heat flux in the FSC case, whereas for the FER simulation, the negative values come from enhanced latent heat fluxes due to stronger winds (Fig. 4).

The zonal wind stress pattern is depicted in Fig. 4. The FSC values are very similar to the FCO ones with even weaker zonal gradients in the western Pacific. The equatorial zonal wind stress has increased by 30% over the 150° – 120° W region in the FER simulation. The northward meridional component has also increased in the equatorial eastern Pacific but is still only half of the observed values just north of the equator (not shown). The change in the convective ER has thus resulted in an increased low-level flow linked to stronger Walker and Hadley circulations. Figure 4c shows intense westerlies over the western equatorial Pacific (west of 160° E) denoting stronger convergence with increased easterlies on the eastern side.

Figure 5 shows the March–May (MAM) precipitation field for the experiments FCO, FSC, and FER and the OBE data. The double ITCZ is already present in forced mode (Fig. 5a) in the control simulation. It is associated to a symmetrical geographical distribution of the rainfall over the entire tropical Pacific resulting in an unrealistic shape for the South Pacific convergence zone (SPCZ). This tendency is maintained in the FSC simulation while it is much weaker in the FER one. In the latter, the ITCZ and SPCZ are well localized with precipitation values

FIG. 2. Latitude–height cross sections of the monthly averaged specific humidity, relative humidity, and total cloudiness differences FER minus FCO (a), (b), (c) for July. In (a) units are in grams per kilogram and contour intervals are every 0.25 g kg^{-1} . In (b), (c) units are in percent and contour intervals are every 2.5%. In all panels, shading corresponds to positive values and the latitude domain is from 60° S to 60° N. The zonal average is performed over the full grid.



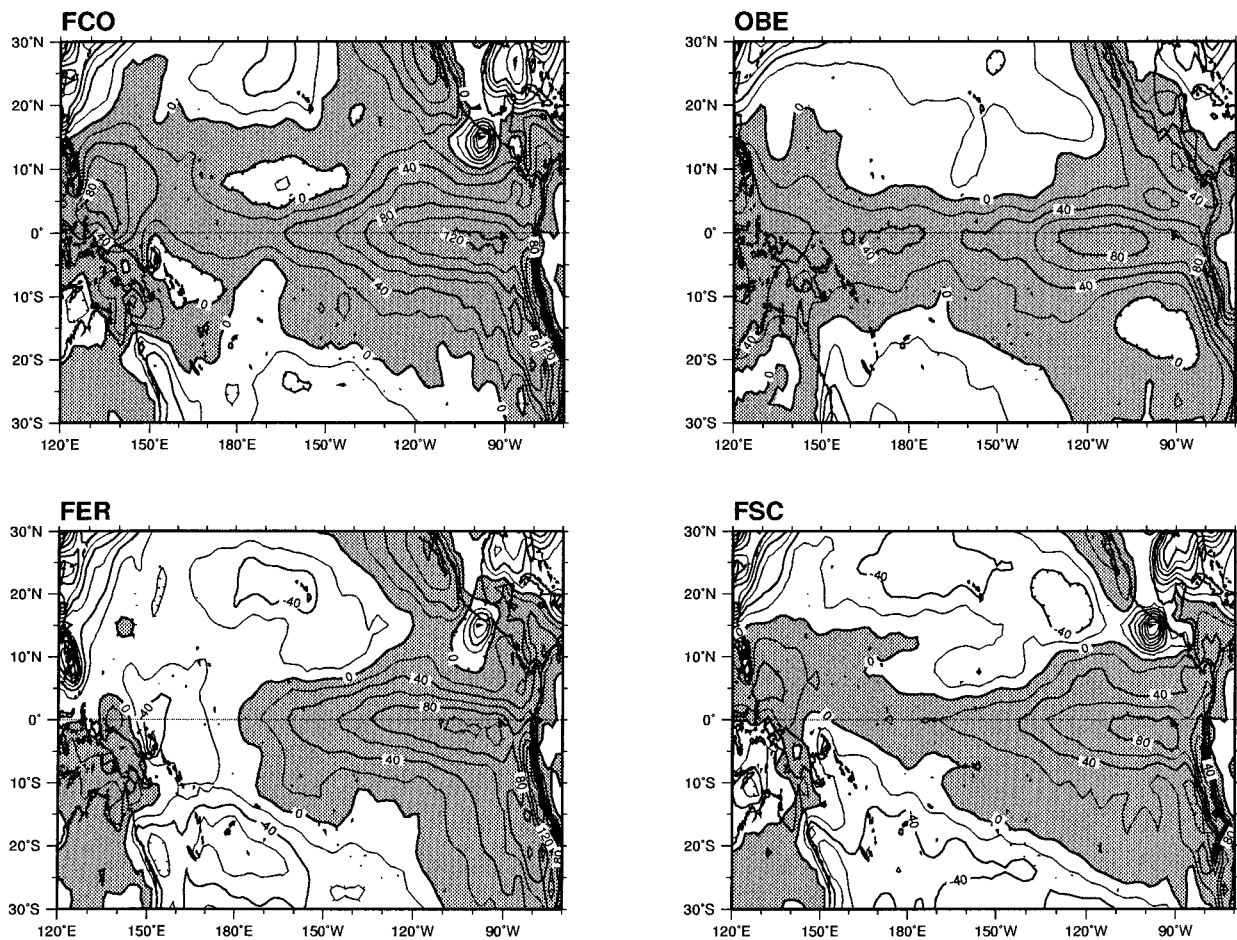


FIG. 3. Geographical distributions of the annual mean total surface heat flux simulated with (a) FCO, (c) FER, (d) FSC, and derived from the OBE dataset (b) between 30°N and 30°S. Fluxes are positive downward. Units are in watts per square meter and contour intervals are every 20 W m^{-2} . Shading corresponds to positive values.

close to the observed ones (greater than the FCO ones over the warm pool). The model even simulates the observed precipitation dipole in the western Pacific and the SPCZ recovers its observed northwest–southeast orientation.

It is worth investigating the mechanisms leading to the remarkable difference between the FCO and FER simulations. Specifically, one needs to understand the transition, regarding the rainfall distribution, between the symmetric FCO and asymmetrical FER states. The precipitation field is related to the vertically integrated diabatic heating due to cumulus convection, large-scale condensation, and radiation processes. In the Tropics, cumulus convection accounts for most of the diabatic heating. It is then quite logical to look at the influence of the FER change on the convective heating and drying profiles. Figure 6 shows latitude–height cross sections of the mean July zonally averaged convective heating and drying rates for the FCO and FER simulations as well as the differences. Both experiments exhibit maximum convective heating in the Tropics with smaller peaks associated to extratropical storm track regions.

The vertical distribution in the Tropics differs markedly between the two experiments: the FER convective heating is much increased north of the equator in the ITCZ with a maximum difference of 1.5 K day^{-1} between 600 and 500 hPa. The increased heating extends from the lower levels to the upper troposphere. The opposite occurs just south of the equator, where the convective heating in the FER simulation is reduced by 0.5 K day^{-1} between 750 and 250 hPa. Figures 6d–f show convective drying of the lower troposphere (up to 850 hPa) for both FCO and FER simulations due to environmental compensating subsidence. The quasi-symmetrical pattern of the FCO experiment is broken in the FER one where relative lower-tropospheric convective moistening and drying occur south and north of the equator, respectively (Fig. 6f). A question regarding the above results is the following. Why is the impact of the ER change so different between regions just north and south of the equator? The direct effect of the ER change on water vapor can be described as follows. At low levels, the main convective contribution to the atmospheric column hu-

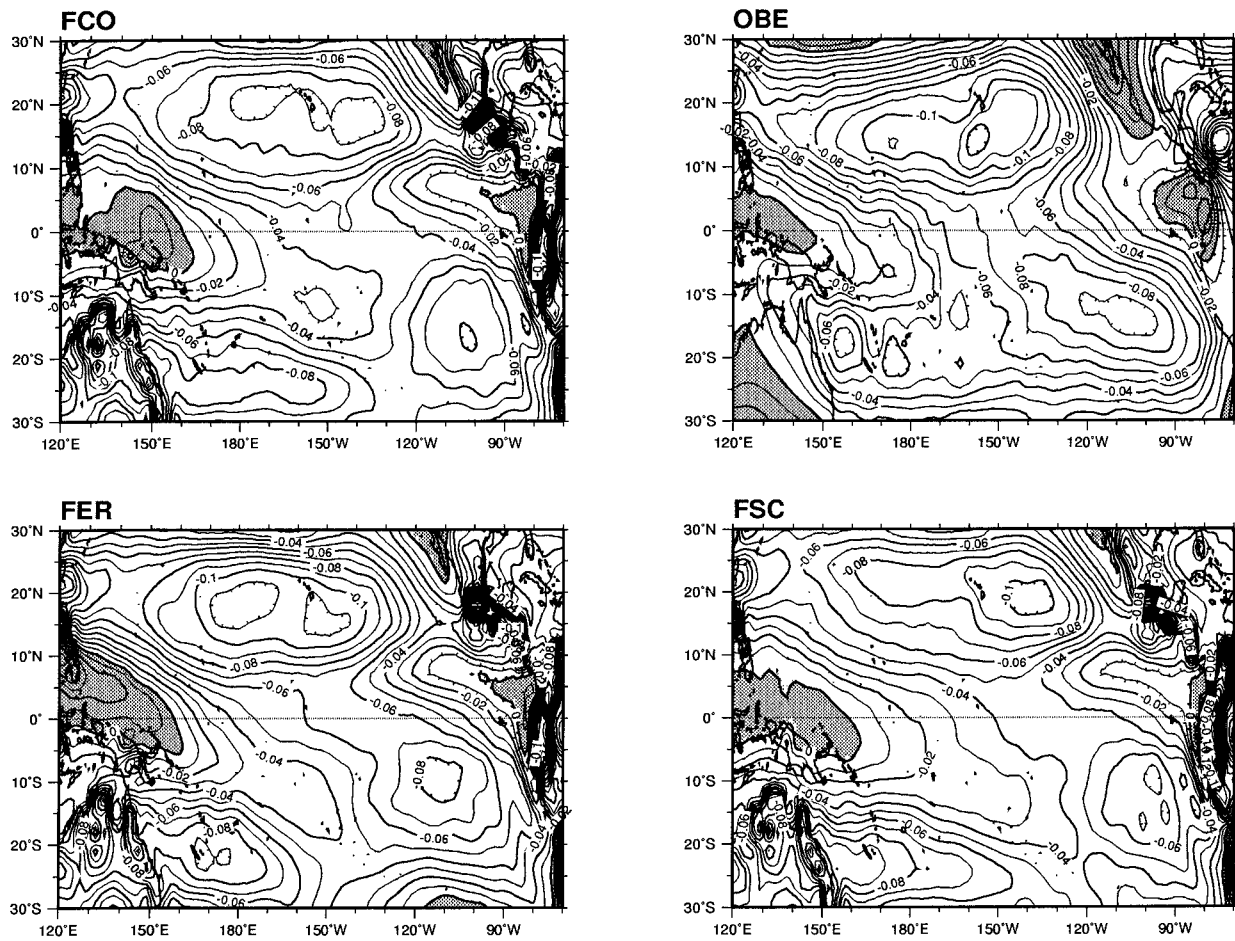


FIG. 4. Geographical distributions of the annual mean zonal wind stress simulated with (a) FCO, (c) FER, (d) FSC, and derived from the OBE dataset (b) between 30°N and 30°S. Units are in pascals and contour intervals are every 10^{-2} Pa. Shading corresponds to westerly winds.

midity budget is given by the mass flux term Q_c (the detrainment term is important only for upper levels):

$$Q_c = -\alpha_k(H_n - H)\frac{\partial q}{\partial p}, \quad (8)$$

where H is the moist static energy of the environment, H_n that of the cloud, p the atmospheric pressure, and α_k a constant determined by the Kuo hypothesis (Bougeault 1985). The ER change gives a stronger relaxation of the temperature and specific humidity cloud values toward the environment at low levels in the moist adiabat determination. Consequently, the upward convective mass flux is reduced at low levels and thus specific humidity increases at the bottom of the convective column. As this direct effect is symmetric (no geographical dependence), the symmetry breaking seen in Fig. 6 must result from a dynamical feedback loop. In the following we investigate changes in the mean atmospheric circulation to demonstrate its existence.

The increase in convective heating in the northern equatorial midtroposphere for the FER simulation is consistent with a vigorous enhancement of the zonally

averaged meridional circulation as shown by Fig. 7. The intensity of the Hadley cell is increased by about 40 and 110 10^9 kg s^{-1} between the two experiments for January and July, respectively. This strengthening of the vertical motions has an impact on the vertical advection of potential temperature. Since potential temperature in the troposphere increases with height and is conserved in adiabatic motions, upward advection leads to colder temperatures in the middle and upper troposphere. So the stronger vertical motions in the FER case tend to produce a cooling in the regions of ascendance compared to the control simulation. This explains the upward extension of the positive relative humidity anomalies in Fig. 2b.

The planetary-scale divergent circulation is also strongly affected by the FER change and can be described in terms of the divergent flow at 200 hPa. Figure 8 presents the mean July divergent flow in terms of the velocity potential χ at 200 hPa for the FCO and FER experiments as well as the European Centre for Medium-Range Weather Forecasts (ECMWF) analysis. Low values of χ denote areas of divergence and therefore

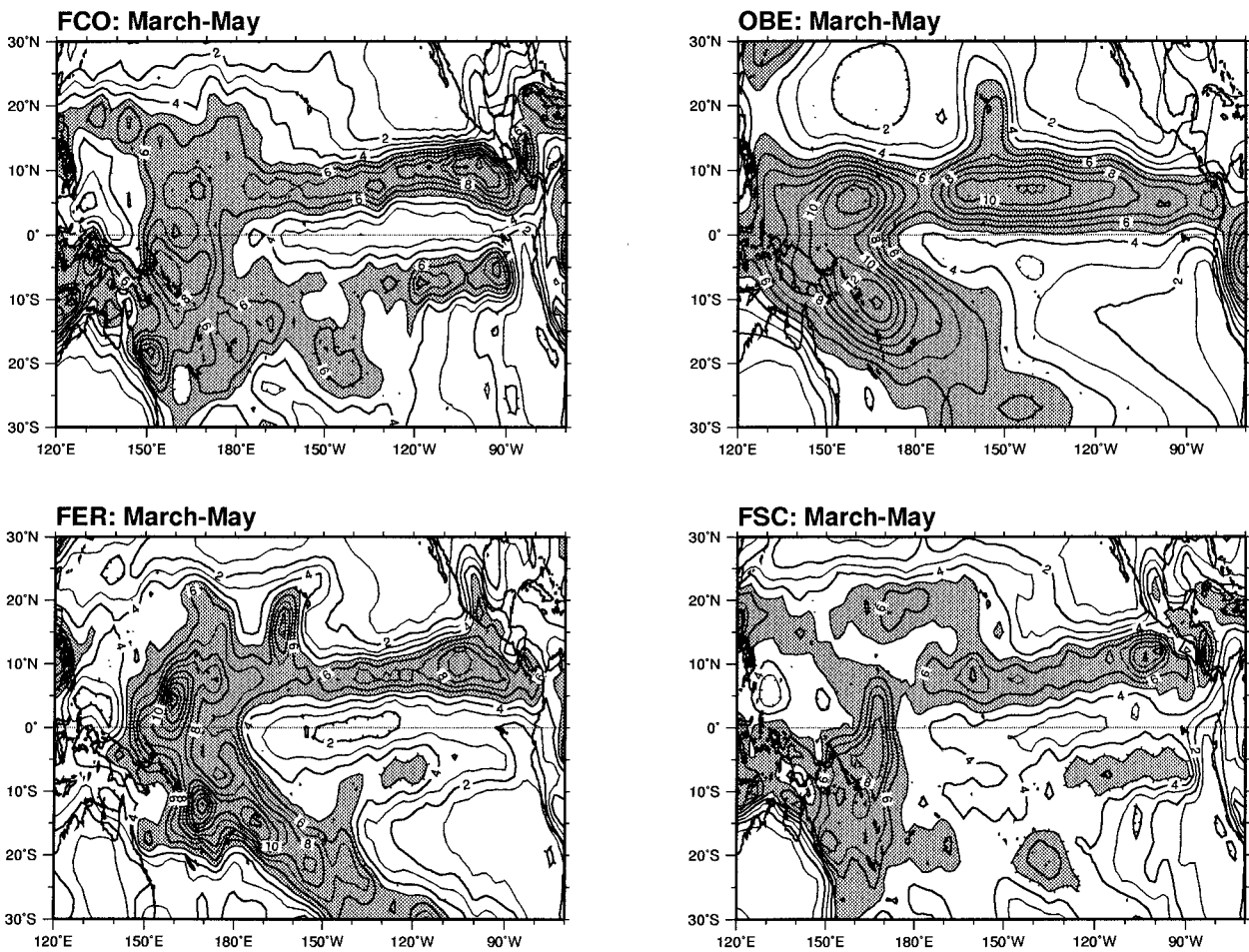


FIG. 5. Geographical distributions of the monthly averaged precipitation for the MAM season simulated with (a) FCO, (c) FER, (d) FSC, and derived from the OBE dataset (b) between 30°N and 30°S. Units are in millimeters per day and contour intervals are every mm day^{-1} . Shading corresponds to values greater than 5 mm day^{-1} .

upward motion below 200 hPa, whereas large values denote convergent flow and downward motion. The FER simulation is characterized by a much stronger upward flow over the western Pacific in good agreement with the analysis results. There is also increased subsidence over South Africa and along the coast of South America, which compares favorably with the ECMWF analysis. Nevertheless, the mean subsidence in the northeastern Pacific is too strong in all the model results compared to those of the analyses and is possibly related to the failure of the model to adequately represent the ITCZ in the eastern Pacific. The stronger zonal circulation in FER is likely to favor vertical mixing of the SST anomalies in the western Pacific and suppress vertical mixing of anomalies in the eastern Pacific.

The stronger Walker and Hadley circulations entail a stronger rising motion, which favors moisture convergence as the rising air must converge at low levels where moisture is abundant. As the change in the moisture transport by the large-scale flow has not been directly estimated, it can be diagnosed from the precipitation P

and the surface evaporation E . For steady-state conditions, as apply for the considered timescale, the moisture convergence M is given by

$$M = P - E. \quad (9)$$

Figure 9 depicts the annual mean moisture convergence for the FCO and FER simulations and for the OBE climatology. The narrow band of moisture convergence situated south of the equator in the central and east Pacific for the FCO experiment disappears in the FER one, which compares fairly realistically with the climatology. More moisture is being advected toward the convergence zones, particularly above the warm-pool region (up to 6 mm day^{-1}), implying a much stronger hydrological cycle.

In summary, the ER change initiates a positive dynamical feedback loop between cumulus convection, the large-scale flow, and moisture convergence. The direct effect of the ER change reduces convection everywhere and, in particular, south of the equator, thereby cooling and increasing low-level humidity within the trade wind

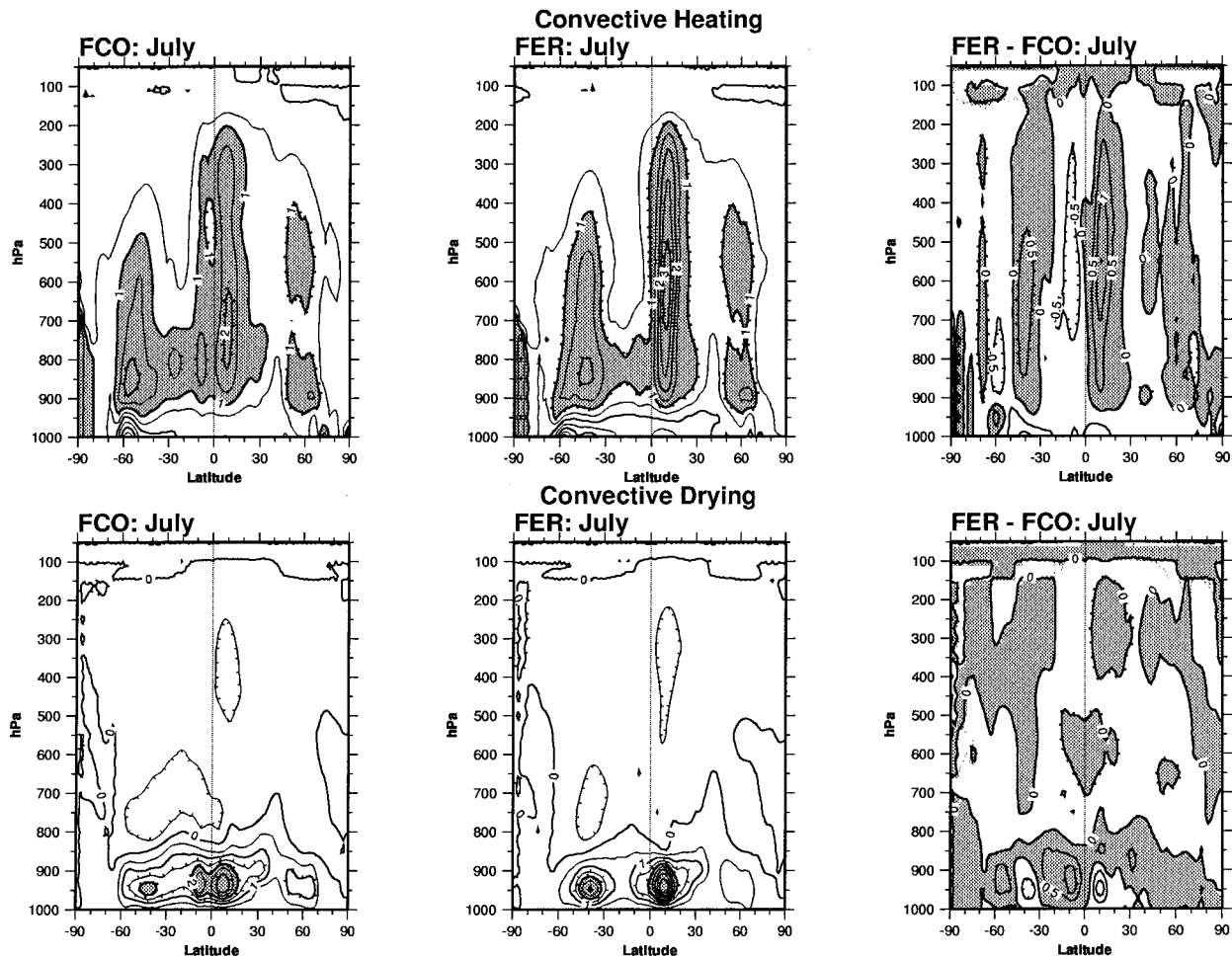


FIG. 6. Latitude–height cross sections of the monthly averaged convective heating and drying rates simulated with (a), (d) FCO; (b), (e) FER; along with their differences FER minus FCO (c), (f) for July. Panels (a), (b), (c) are heating rates and (d), (e), (f) drying rates. In (a), (b), (c) units are in kelvins per day and contour intervals are every 0.5 K day⁻¹. Shading corresponds to values greater than 1 K day⁻¹ (to positive values for the difference field). In (d), (e), (f) units are in grams per kilogram per day and contour intervals are every 0.5 g kg⁻¹ day⁻¹. Shading corresponds to values greater than 2 g kg⁻¹ day⁻¹ (to positive values for the difference field, which indicate moistening). The zonal average is performed over the full grid.

cumulus layer. This additional supply of moisture is then available for horizontal transport into the tropical convergence zones through the mean trade wind flow. It yields an increased moisture convergence into the deep convection areas, such as the ITCZ, due to the additional water vapor transport from neighboring latitudes. This indirect dynamical effect overcomes the direct effect, resulting in a strongly asymmetric profile for the heating and drying convective rates. Therefore, these simulations suggest a strong link between the PBL structure in the southeast Pacific and the asymmetry of the atmospheric state. The modified convective entrainment helps to maintain the PBL structure in the trade wind areas by providing cooling and moistening to balance the drying and warming effect of subsiding large-scale motions. A similar effect might be obtained by slightly changing the convection scheme closure. As mentioned above, the dry bias is due to the lack of selectivity in

the application of the convection scheme. Imposing an additional constraint—for instance, a threshold over the mean relative humidity in the cloud layer (Gregory 1994)—could lead to better-defined convergence zones and improved transient activity.

The added cloud and modified convection schemes do significantly affect heat, momentum, and mass surface fluxes, which are driving the ocean in coupled mode. It is then interesting to see how coupled ocean–atmosphere feedbacks may modify the patterns observed in the forced simulations and to study the impact of atmospheric changes on the ocean climatology.

b. Coupled experiments: CCO, CSC, and CER

Figure 10 displays the annual mean SST maps for the CCO, CSC, and CER simulations as well as the OBE data. The most remarkable feature is the inversion, in

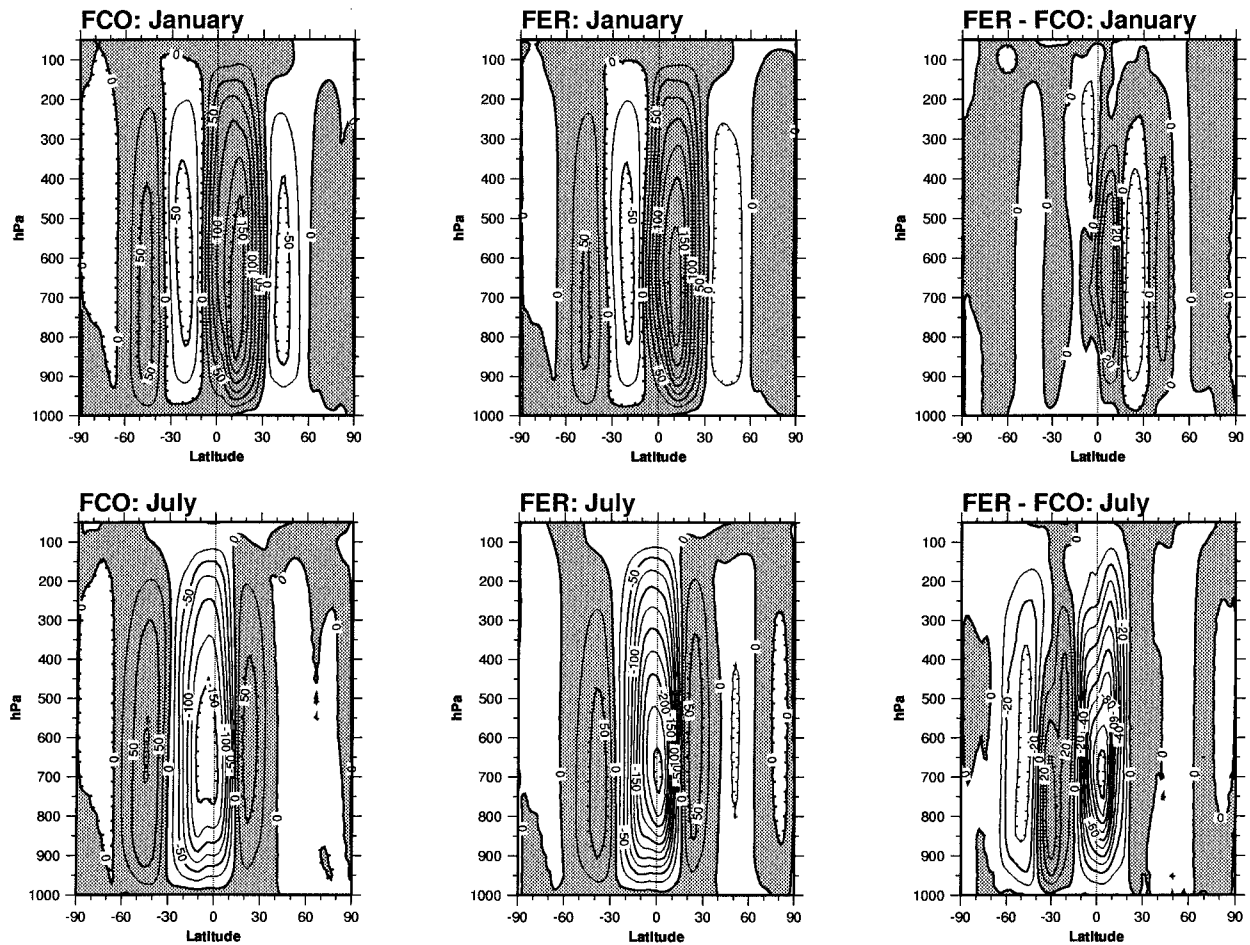


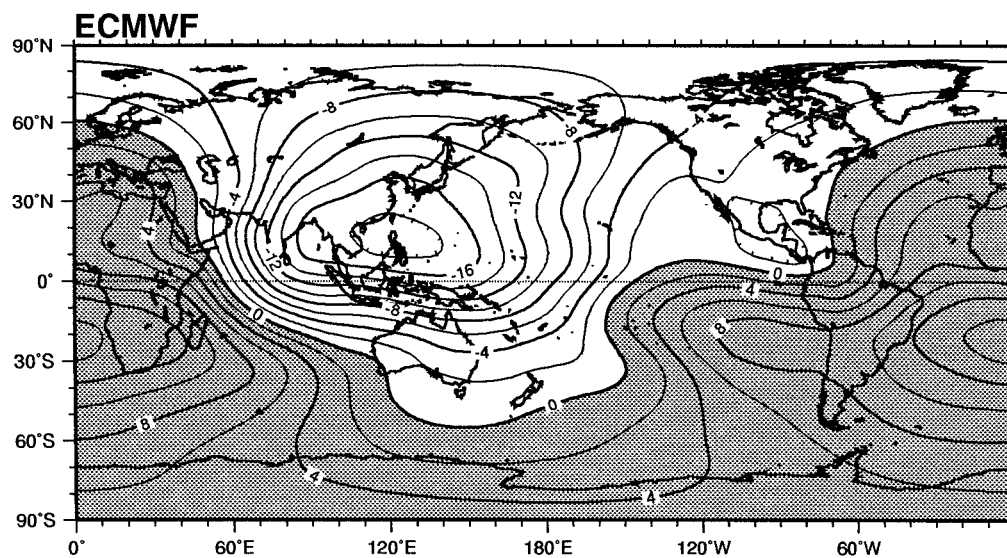
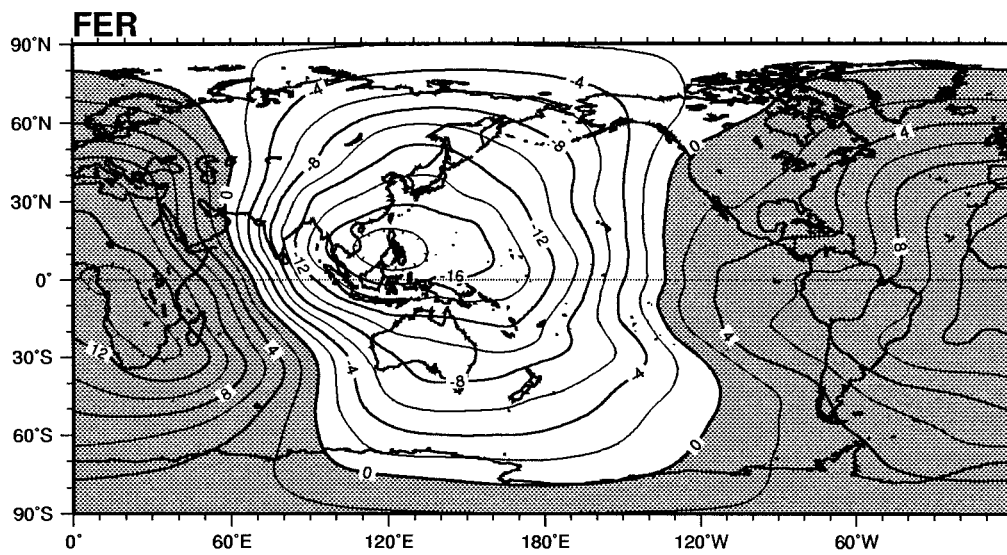
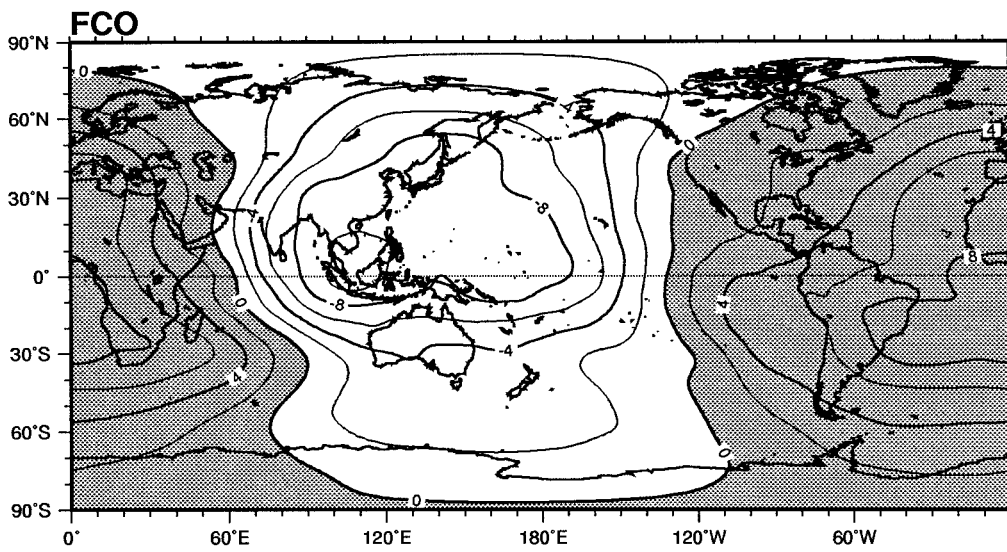
FIG. 7. Latitude–height cross sections of the monthly averaged mean meridional circulation simulated with (a), (d) FCO; (b), (e) FER; along with their differences FER minus FCO (c), (f) for January and July. Panels (a), (b), (c) are January and (d), (e), (f) are July. Units are in 10^9 kg s^{-1} and contour intervals are every $25 \text{ } 10^9 \text{ kg s}^{-1}$. Shading corresponds to positive values. Clockwise and counterclockwise circulations are indicated by positive and negative values for the streamlines, respectively. The zonal average is performed over the full grid.

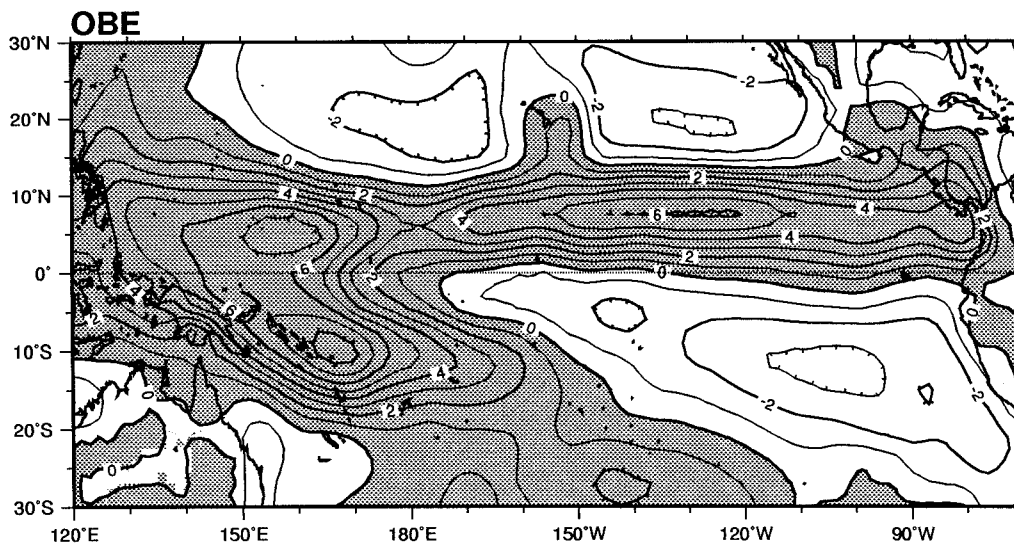
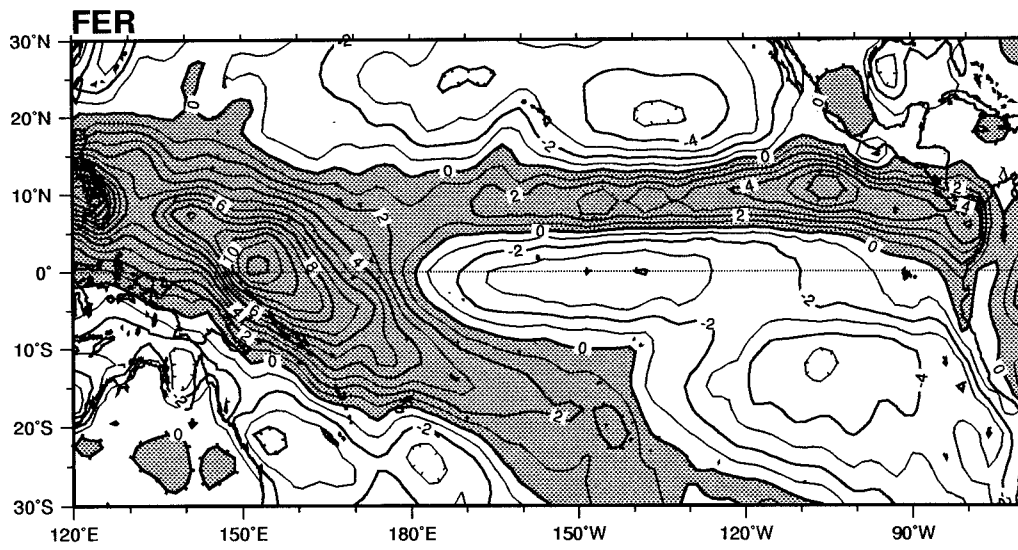
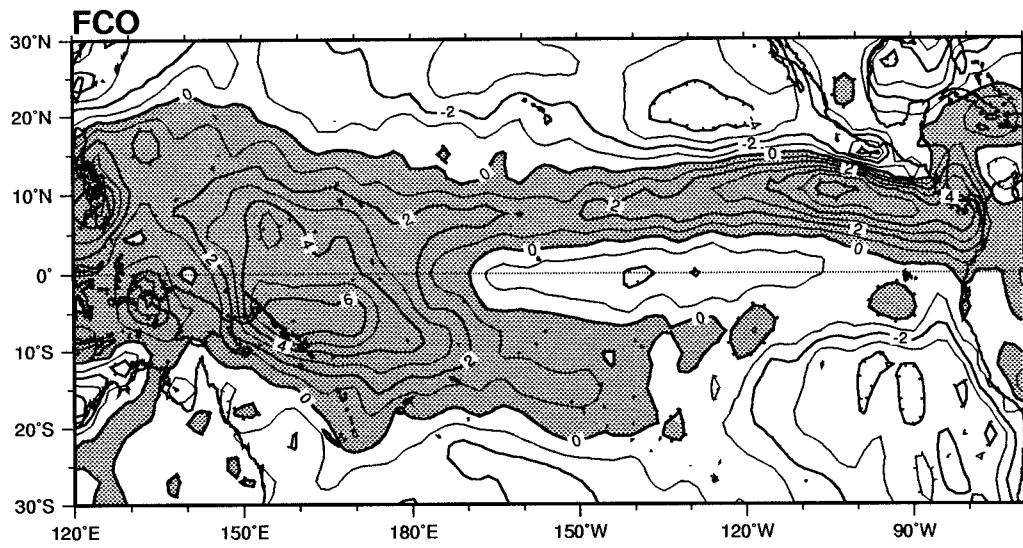
the CER simulation, of the warm bias present in the CCO experiment over the central and eastern Pacific. The cold tongue extends westward into the western Pacific and strongly erodes the warm pool. The waters along the North Equatorial Counter Current (NECC) are 1°C colder in the CER simulation. A similar cold pattern, though much less marked, is obtained with the CSC experiment. The warm pool keeps a reasonable shape but with a temperature 1°C colder and the cold waters along the South American coast are well simulated. To summarize, both CER and CSC show a more realistic representation of the zonal SST gradient as well as the cold tongue in the eastern Pacific. However, they both fail to produce a realistic warm pool as far as its shape (CER) and temperature (CER and CSC).

Figure 11 shows similar maps for the mean precipitation fields. The anomalous precipitation band around 5°S in the eastern Pacific, present in both CCO and CSC, is strongly reduced in the CER simulation. In the latter, the convection cell over the warm pool area, which was moved eastward in CCO, is being displaced westward of its observed position. This displacement is related to the strong equatorial cooling over the central and western Pacific. The dry zone over the central Pacific is also accurately depicted. The precipitation amount is underestimated over the tropical convergence zones for the three simulations compared to the OBE values.

The mean zonal wind stress is presented in Fig. 12 for the three simulations and the OBE data. Comparison between CCO and CER shows strikingly different spa-

FIG. 8. Geographical distributions of the annual mean 200-hPa velocity potential simulated with (a) FCO, (b) FER, and derived from the ECMWF data (c) between 90°N and 90°S . The ECMWF data are the annual mean for the 1985–91 analysis period. Units are in $10^6 \text{ m}^2 \text{ s}^{-1}$ and contour intervals are every $10^6 \text{ m}^2 \text{ s}^{-1}$. Shading corresponds to positive values (indicative of convergence).





tial patterns in the equatorial Pacific. The CER simulation shows values almost twice as strong as the CCO ones in the 165°–120°W region (always greater than 0.05 Pa). The westerlies have been displaced west of 120°E in the CER simulation, whereas they extend until 170°E in the control one. Slightly stronger values are also depicted in CER for the trades core regions. The southeast trades maximum position is realistically simulated in CCO and CER. The northeast trades simulated dipole in CCO becomes a more intense monopole centered at 20°N–180°, which is westward and northward of the climatological one (15°N–150°W). The CSC simulation shows values in between CCO and CER in the central Pacific region (around 0.04 Pa) and the same pattern as CER in the western Pacific (with weaker easterlies).

In summary, the performance of the coupled GCM is highly sensitive to changes in the parameterization of convective entrainment rate. The standard version gives a steady state (which resembles an El Niño with warm SSTs in the central and eastern Pacific), weak easterlies over the central equatorial Pacific, and an anomalous convergence zone south of the equator in the eastern Pacific. On the opposite, the modified version simulates a mean state similar to a La Niña state with an enhanced cold tongue, which extends too far to the west relative to observations. The easterlies prevail over the entire equatorial Pacific with realistic amplitude in the center of the basin. The convergence zones are accurately depicted although the tropical heat source in the western Pacific has shifted westward. To summarize, the CER simulation appears more *realistic* than the CCO one and is particularly interesting as the systematic biases generally found in tropical CGCMs (double or migrating ITCZ, warm SSTs in the southeast Pacific) are absent. The coupled GCM is also sensitive to the parameterization of SC clouds. The CSC simulation gives SSTs values in good agreement with the OBE climatology, whereas the precipitation and the zonal wind stress share qualitatively the same biases as CCO (with reduced amplitude). The quite remarkable contrast between the climatologies of the CCO, CER, and CSC experiments is suggesting that differences in the relative magnitude of coupled feedbacks within the CGCM can lead to strikingly different climate drifts.

4. Coupled processes impact on climate drift

In this section and following Dijkstra and Neelin (1995), the “climatological version of the Bjerknes hypothesis,” namely, that coupled ocean–atmosphere pro-

cesses strongly influence the spatial structure of the tropical Pacific climatology, is investigated with the CGCM simulations of the previous section. Specifically, reasons are sought for the drastic differences noted in the CCO, CER, and CSC simulations of the warm pool–cold tongue structure within the equatorial Pacific. Before diagnosing the physical processes fundamental to either climate drifts, some insight can be gained by simply looking at the SST difference maps between the modified and control experiments (Fig. 13). The CER map (Fig. 13a) shows differences located mainly within a narrow equatorial band across the Pacific Ocean and along the South American coast. The maximum cooling occurs on the equator around 100°W with a value of 3°C. The CSC cooling is weaker in the western Pacific and stronger over the anticyclonic regions of the subtropical Pacific Ocean (Fig. 13b). The cooling maxima (4°C) are situated along the Californian and Peruvian coasts away from the equator. The different cooling patterns indicate that different mechanisms or differences in process amplitudes are operating between the CER and CSC experiments.

a. Surface forcing and atmospheric boundary layer

The first idea is whether the different SST distributions simply reflect different total heat fluxes at the ocean surface. The CER total heat flux deviation map shows strong positive values (up to 40 W m⁻² at 100°W) in the equatorial wave guide (5°S–5°N) (Fig. 13c) due to an increase in solar irradiance. The latter is associated with the decrease in cloudiness due to reduced convection linked with the colder equatorial SSTs. Furthermore, the total heat flux anomaly resembles the negative of the SST anomaly, which suggests that the atmosphere is reacting as a negative feedback to the SST cooling.

In the central and eastern Pacific, the CSC total heat flux deviation map shows small positive values within the 5°S–5°N lat band (Fig. 13d). Large negative values are depicted in the eastern subtropics indicating a strong reduction in solar radiation due to the enhanced simulated stratus deck (not shown). These negative anomalies do correspond in sign to the SST anomalies, which suggest that the observed cooling can be, at least partly, attributed to the diminished total heat flux in these regions.

To study the coupling impact on PBL physics, distributions of sea–air temperature difference ($SST - T_{s}^{air}$) and surface relative humidity are compared to suggest possible mechanisms for the changes in total heat flux and precipitation surface budgets (Fig. 14). The

←

FIG. 9. Geographical distributions of the annual mean excess M of precipitation over surface evaporation simulated with (a) FCO, (b) FER, and derived from the OBE dataset (c) between 30°N and 30°S. Under steady conditions, M represents the net moisture supply through lateral advection as well as runoff. Units are in millimeters per day and contour intervals are every mm day⁻¹. Shading corresponds to positive values (indicative of moisture convergence).

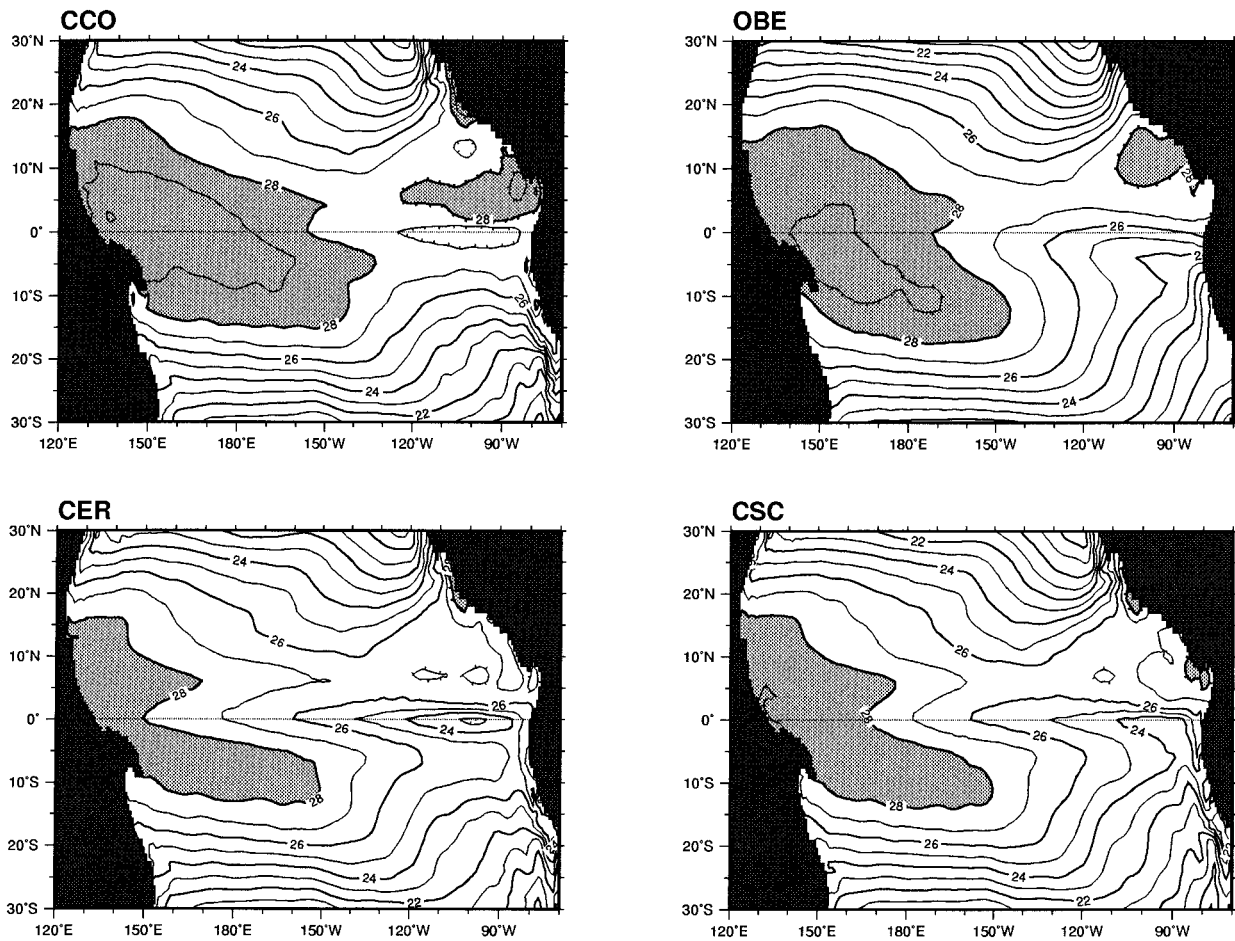


FIG. 10. Geographical distributions of the annual mean sea surface temperature simulated with (a) CCO, (c) CER, (d) CSC, and derived from the OBE dataset (b) between 30°N and 30°S. Units are in Celsius and contour intervals are every 1°C. Shading corresponds to values greater than 28°C.

former gives a crude measure of atmospheric boundary layer stability, whereas the latter is indicative of the surface moisture field (Deser and Wallace 1990). Positive values for $(SST - T_s^{air})$, indicative of unstable conditions, are depicted in the equatorial Pacific for the CCO simulation with large values over the eastern ITCZ and warm-pool areas. Negative sea-air temperature differences are simulated over the equatorial cold tongue in the CER simulation. A stable boundary layer (values less than -0.25°C) is present on and south of the equator between 90° and 160°W. The ITCZ is well defined with positive values greater than 0.25°C across the whole Pacific. The CSC simulation shows large negative values over the cold upwelling regions (both the coast of Peru and the equatorial cold tongue). Stable conditions are also present in the central Pacific along the ITCZ indicating reduced convection. Coupled ocean-atmosphere feedbacks are clearly responsible for the observed differences as the sea-air temperature difference field is very similar between the three forced experiments (not shown). For instance low-cloud lock-in

(Randall 1994) can lead to a SST cooling in the CSC simulation. Increased cloudiness reduces surface insolation, which cools the underlying ocean surface. The colder SSTs give increased atmospheric boundary layer stability, which traps water vapor near the surface, thereby raising low-level relative humidity and cloudiness. This mechanism is probably effective along the Peruvian coast in the CSC simulation as shown by the higher relative humidities compared to CCO (Figs. 14d-f). However other boundary layer processes must be present as evidenced by the corresponding CER map (Fig. 14e), which depicts larger values over the equatorial eastern Pacific and along the ITCZ. Regions of stable stratification are characterized by high surface relative humidities as vertical mixing of moisture is inhibited within the atmospheric boundary layer. The surface moisture difference between CER and CSC is then not consistent with the corresponding difference in atmospheric boundary layer stability for the eastern Pacific region. As surface evaporation is roughly the same in the two simulations, the discrepancy could be explained

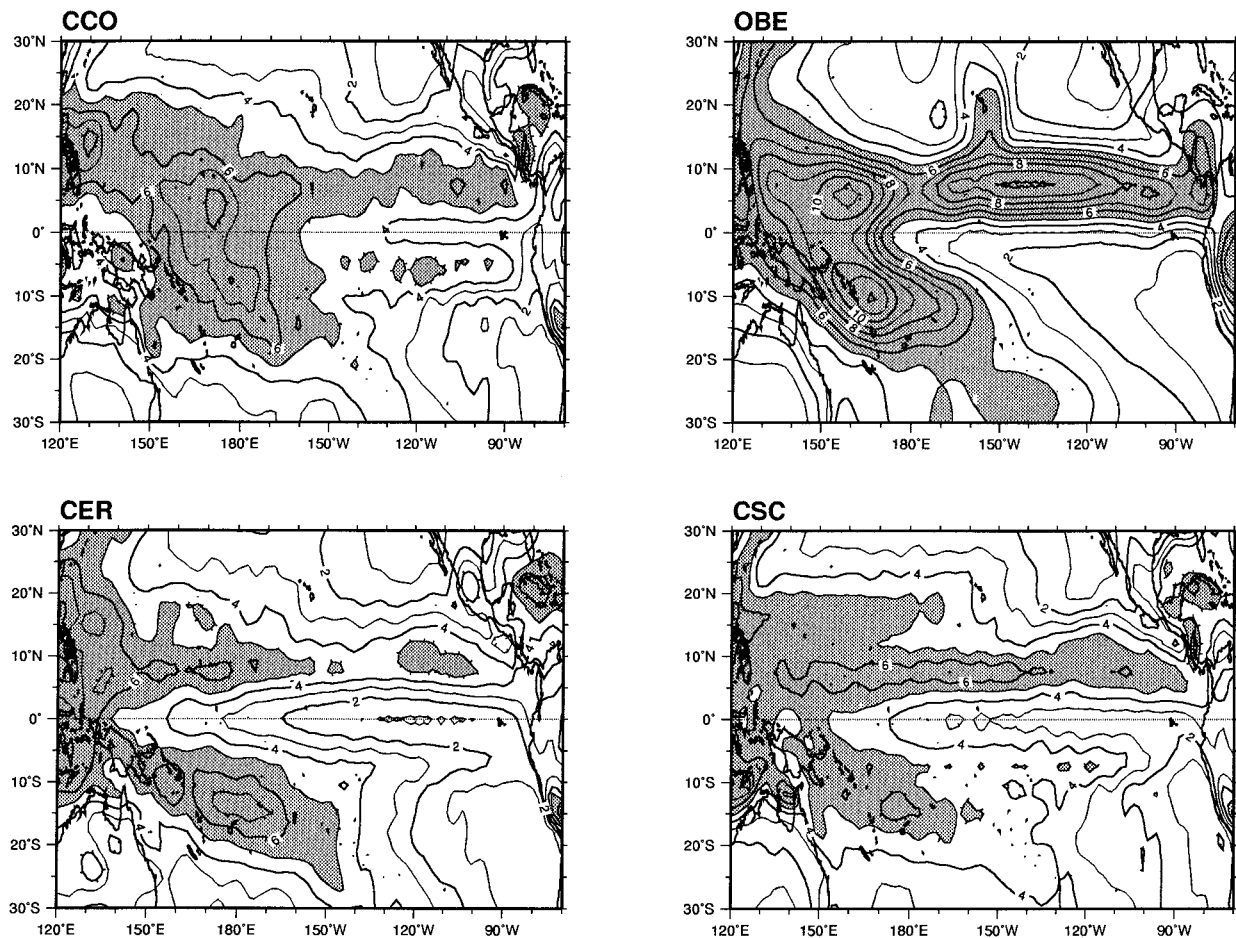


FIG. 11. Geographical distributions of the annual mean rainfall simulated with (a) CCO, (c) CER, (d) CSC, and derived from the OBE dataset (b) between 30°N and 30°S. Units are in millimeters per day and contour intervals are every mm day^{-1} . Shading corresponds to values greater than 5 mm day^{-1} .

by stronger upper PBL mixing with the drier free atmosphere in the CSC case. This is coherent with a stronger deep convective activity in the southeastern Pacific. This stronger ventilation of the PBL could also result from a more active shallow convection in the CSC simulation. The intensity of shallow convection is related to the saturation deficit gradient, which has larger values in the CSC case from the upper part of the PBL to the midtroposphere, especially south of the equator (not shown). This suggests the following interpretation: both shallow and deep convection strive to maintain drying of the lower atmosphere by pumping moisture out of the PBL and feeding it into the free atmosphere. This, in turn, maintains a high evaporation rate, thereby contributing to the moisture convergence, which drives the mass flux scheme. This mechanism could explain the maintenance of a double ITCZ in CSC (although the SSTs are much colder than in CCO) while it clearly weakens in CER.

In summary, the simulated sea surface cooling cannot be solely explained through changes in atmospheric heat forcing at least for the CER case. To gain a deeper

insight into the physical processes involved with the cooling, one has to analyze dynamical and thermal changes in the ocean upper layers. Furthermore, shallow convection likely plays an important role in the maintenance of the double ITCZ through a positive feedback with the deep convection and surface evaporation.

b. Upper-ocean description

1) MEAN ZONAL AND MERIDIONAL CIRCULATION

Figure 15 shows an equatorial section of the annual mean zonal current and vertical velocity for the CCO, CER, and CSC simulations. The surface westward flow, driven by the mean winds, strongly increases in both CSC and CER experiments with a maximum of 35 cm s^{-1} reached in the CER case. The mean flow is westward along the whole equatorial Pacific, but it is eastward from the western part of the basin until 160°W in the control simulation. The three simulations do represent a subsurface current, sloping toward the eastern part of the basin, the equatorial undercurrent (EUC). The latter

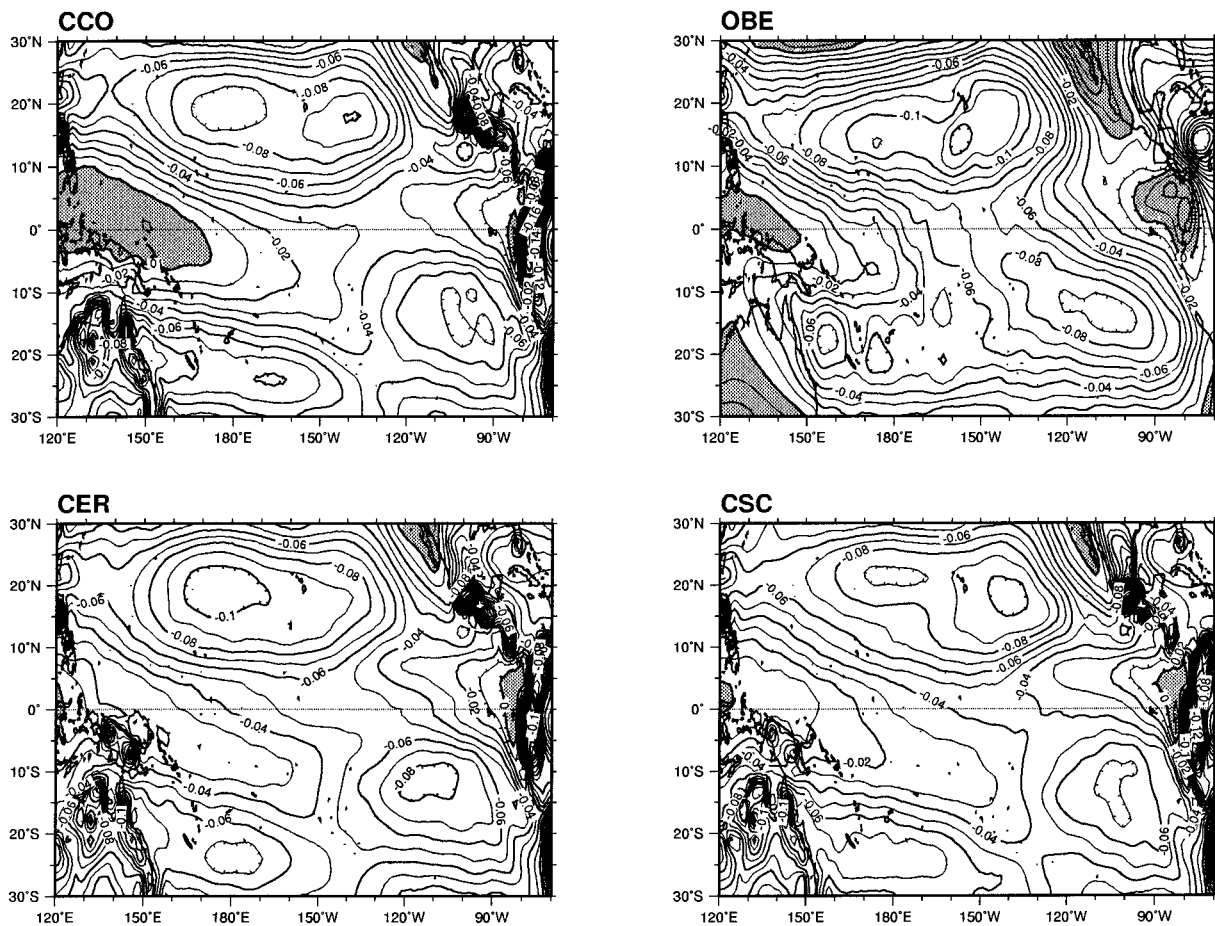


FIG. 12. Geographical distributions of the annual mean zonal wind stress simulated with (a) CCO, (c) CER, (d) CSC, and derived from the OBE dataset (b) between 30°N and 30°S. Units are in pascals and contour intervals are every 10^{-2} Pa. Shading corresponds to westerly winds.

is due to the pileup of warm surface-layer waters in the western Pacific under the action of trade wind-driven westward mean currents. This creates a zonal pressure gradient that accelerates the fluid eastward in the subsurface. Nevertheless, there are substantial differences between the three simulations. While the EUC maximum velocities are relatively close [$U_{\max}(\text{CER}) = 1.20 \text{ m s}^{-1} > U_{\max}(\text{CSC}) = 1.12 \text{ m s}^{-1} > U_{\max}(\text{CCO}) = 1.07 \text{ m s}^{-1}$], the position of the EUC core relatively to the 20° isotherm depth as well as the upper vertical shear strongly differ between the three simulations. The EUC core is located above the thermocline (taking the 20° isotherm depth as a good indicator of its mean position) in CCO while it is found in the middle of it in both CER and CSC. This is primarily due to the much stronger tilt of the thermocline slope in the CER and, to a lesser degree, CSC case. The steepening of the thermocline slope is associated to the strong increase in zonal wind stress over the central Pacific (180°–110°W) (Fig. 12). Additionally, a deepening and a westward shift of the EUC core are observed in both CER and CSC.

A recent numerical study performed by Maes et al. (1997) has identified the various EUC dynamical regimes simulated with the OPA model. In particular, the upper EUC regime exhibits a balance between, on one hand, the zonal pressure gradient and vertical advection terms (EUC acceleration) and on the other hand, the vertical diffusion and horizontal advection terms (EUC deceleration). Moreover, the contribution of these terms do vary according to their vertical scale. These results can be used to provide a qualitative explanation for the changes in EUC core location mentioned above. The zonal pressure gradient strongly increases for both CER and CSC as well as its vertical scale due to the enhanced equatorial wind stress in the central Pacific. Similarly, the enhanced mean upwelling in the (180°–110°W; 80–120 m) longitude–depth box does increase the efficiency of the vertical advection term [$w(\partial u)/(\partial z)$] in this region. These two processes could lead to the observed deepening and westward shift of the EUC core in the CER and CSC experiments.

The subsurface flow reversal in the west of the basin (eastward in CCO and westward for both CER and CSC)

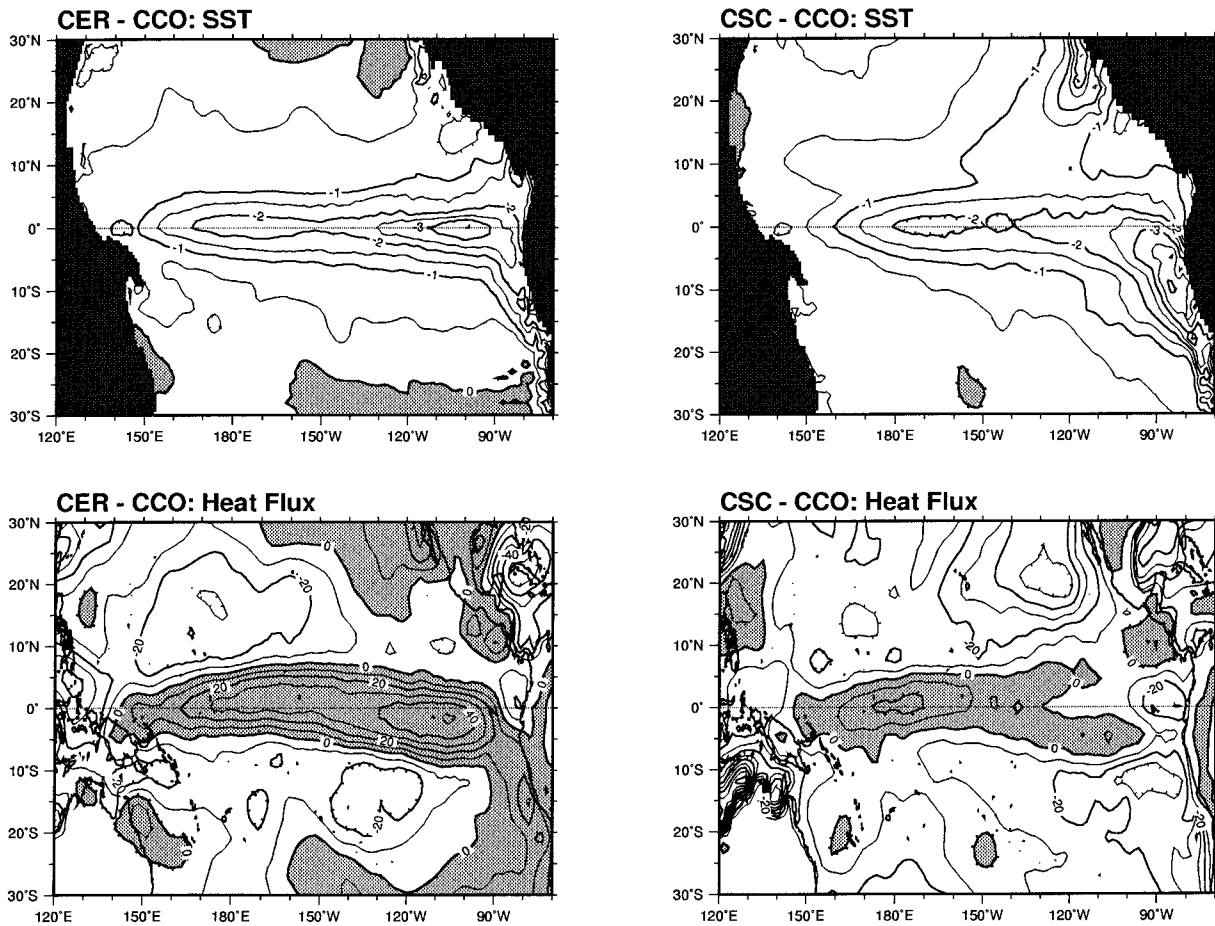


FIG. 13. Geographical distributions of the annual mean sea surface temperature and total surface heat flux differences (from the control simulation CCO) simulated with (a), (c) CER and (b), (d) CSC. In (a), (b), units are in Celsius and contour intervals are every 0.5°C. In (c), (d), units are in watts per square meter and contour intervals are every 10 W m⁻². Shading corresponds to positive values and heat fluxes are positive downward.

can be partly explained by the rise in vertical scale of the vertical diffusion term. Strong easterlies and increased vertical velocity shear (linked to the westward surface flow induced by the winds) are sources of TKE and lead to a deeper mixed layer in both CER and CSC. The decelerating effect of the vertical diffusion reaches deeper depths and balances the zonal pressure gradient term between the 60- and 100-m depths around 165°E.

Furthermore, important differences are found in the amplitude [$W_{\max}(\text{CER}) = 3.21 \text{ m day}^{-1} > W_{\max}(\text{CSC}) = 2.95 \text{ m day}^{-1} > W_{\max}(\text{CCO}) = 2.38 \text{ m day}^{-1}$] and location of the upwelling along the equator. Strong values (greater than 2 m day⁻¹) are found within the thermocline (around and below the 20°C isotherm depth) in CER and, to a lesser degree, in CSC. However, in the control simulation, significant values are depicted only well above the thermocline. So the mean upwelling can access much colder water in both CER and CSC relatively to CCO, especially in the eastern Pacific. In the central Pacific, it has slightly greater values for the

CCO case in the upper layers while it reaches deeper depths for both CER and CSC.

The meridional structure of the zonal current and vertical velocity at 150°W is illustrated on Fig. 16. The CCO equatorial current structure is quite symmetric with a very weak South Equatorial Current (SEC) (maximum velocity is $U_{\max} = 0.14 \text{ m s}^{-1}$) and the existence of a South Equatorial Counter Current (SECC) between 2° and 6°S. The simulated EUC is relatively sluggish with a maximum velocity of 0.7 m s⁻¹ at 120 m depth. The CER and, to a lesser degree, the CSC simulations do exhibit a more active equatorial dynamics with much stronger SEC and EUC (maximum velocities of 0.48 m s⁻¹ and 1.06 m s⁻¹, respectively, in the CER case). Nonetheless, the CSC experiment still shows a pattern with symmetric features such as the presence of a SECC and the separation of the SEC in two asymmetric branches not as marked as in the CER case.

Equatorial upwelling, which is controlled by divergence of the meridional flow exhibits weak values (<1

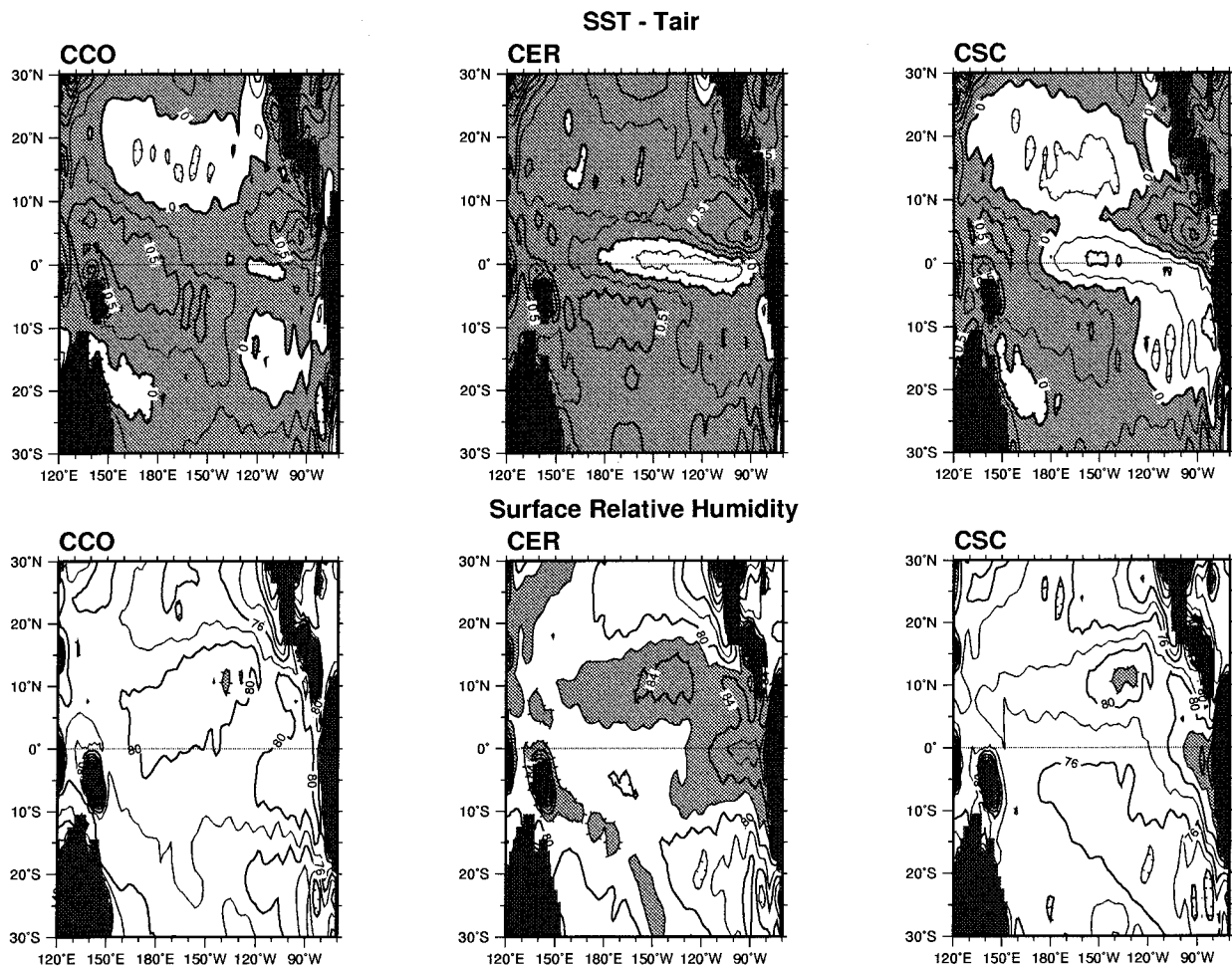


FIG. 14. Geographical distributions of the annual mean sea–air temperature difference (defined as $SST - T_{air}^{surf}$) and surface relative humidity simulated with (a), (d) CCO; (b), (e) CER; and (c), (f) CSC. Panels (a), (b), (c) are sea–air temperature differences and (d), (e), (f) are surface relative humidities. In (a), (b), (c), units are in Celsius and contour intervals are every 0.25°C . Shading corresponds to positive values. In (d), (e), (f), units are in percent and contour intervals are every 2%. Shading corresponds to values greater than 82%.

m day^{-1}) in the upper 50 m for all three simulations. Higher values are found at deeper depths for the CER experiment ($>1.5 \text{ m day}^{-1}$ between 80- and 120-m depths).

2) UPPER-OCEAN THERMAL STRUCTURE

As shown in the previous section, changes in the equatorial zonal wind stress have significantly altered the ocean dynamics between the CCO, CSC, and CER simulations. Similarly, the equatorial ocean thermal structure has been deeply modified as depicted in Fig. 17. The warm-pool margin shifts westward in CSC and is pushed close to the western boundary in CER. The warm-pool volumic extension is greatly reduced in the CER and, to a lesser degree, CSC simulations. As already seen, they both exhibit a sharp increase in the thermocline slope eastward of 150°W and a strong surface cooling in the eastern part of the basin. These conditions lead to stronger zonal equatorial SST gradients

in CER and CSC compared to CCO. These results are mutually consistent with our previous atmospheric findings such as the wind stress increase around 150°W , the low-level flow reversal in the western Pacific, and the diminished solar radiation in the far eastern Pacific for the CSC simulation. While the western Pacific mixed layer is cooler in CER and CSC, its depth strongly increases, as stated previously and clearly seen in Fig. 17, leading to a vertical warm–cold dipole in the temperature difference fields (Fig. 18).

c. Discussion

Relying on simple model analysis, changes in the relative amplitude of coupled feedbacks are sought to qualitatively explain the differences between the simulated climatologies. What are the main processes setting the position and spatial pattern of the warm pool–cold tongue complex? As demonstrated in Dijkstra and Neelin (1995) for a simple model, the balance between

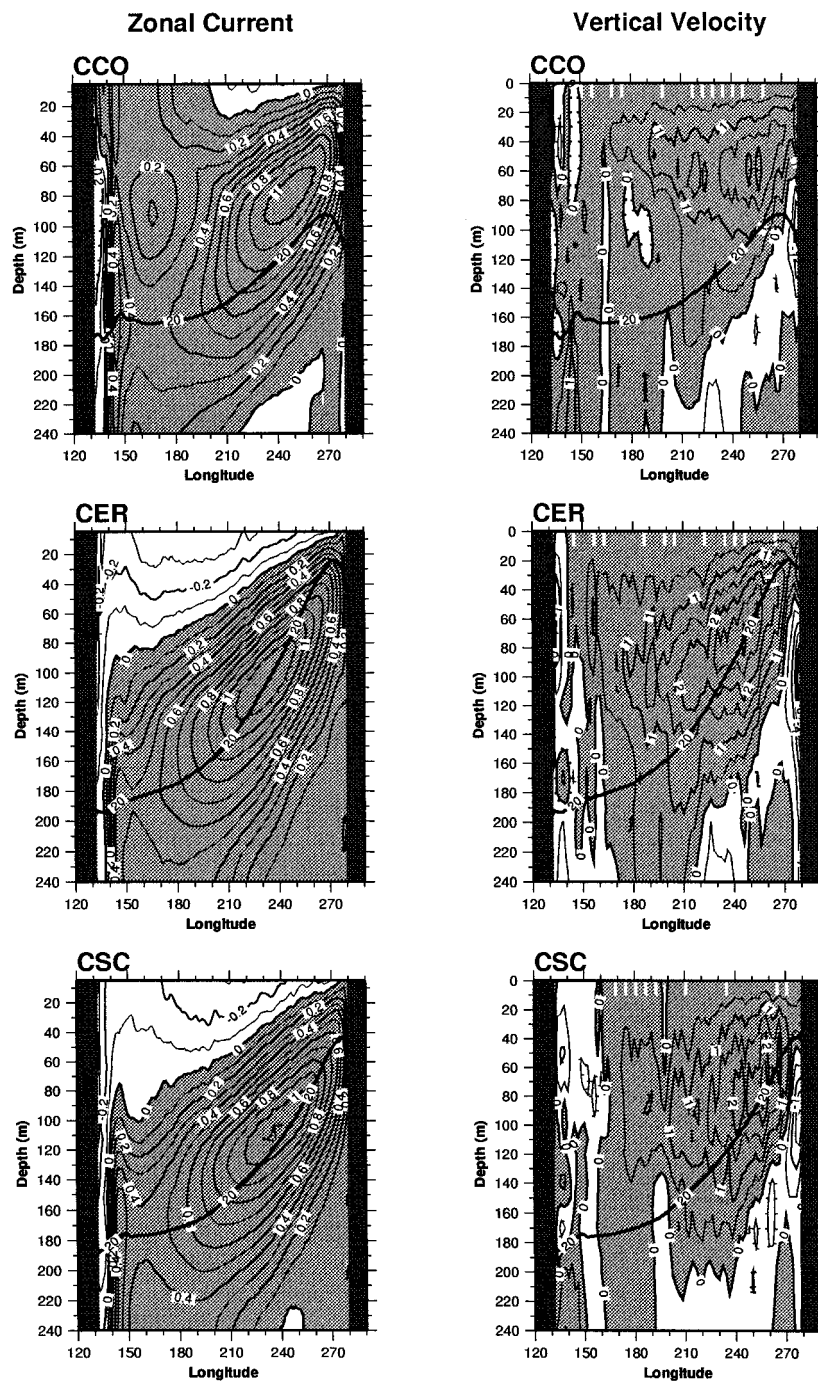


FIG. 15. Equatorial depth-longitude sections of annual mean zonal current velocity and vertical velocity simulated with (a), (b) CCO; (c), (d) CER; and (e), (f) CSC. Panels (a), (c), (e) are zonal current velocities and (b), (d), (f) are vertical velocities. In (a), (c), (e) units are in m s^{-1} and contour intervals are every 0.1 m s^{-1} . Shading corresponds to positive values, i.e., eastward currents. In (b), (d), (f), units are in m day^{-1} and contour intervals are every 0.5 m day^{-1} . Shading corresponds to positive values, i.e., upwelling. In all figures, the thick solid line represents the relevant 20°C isotherm.

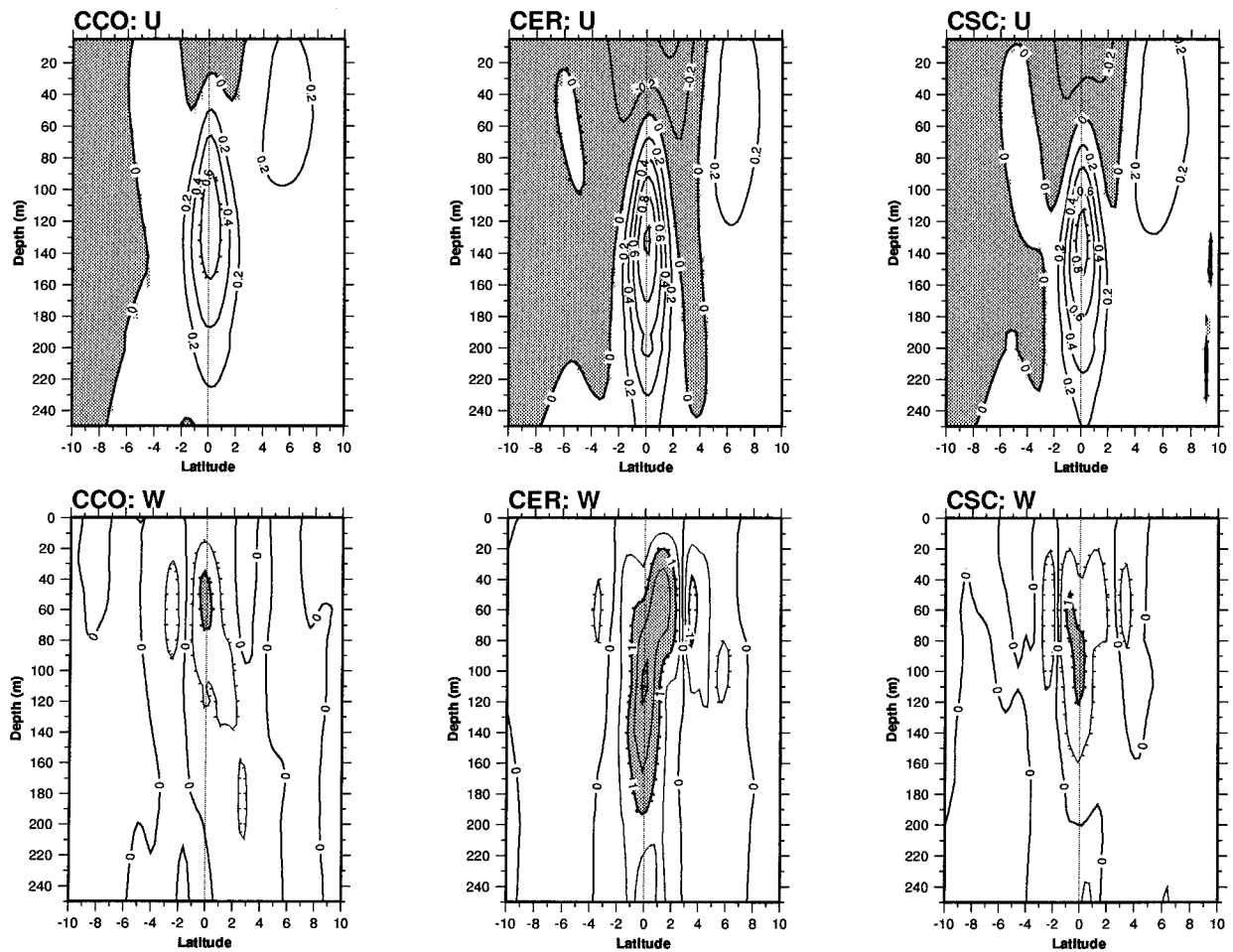


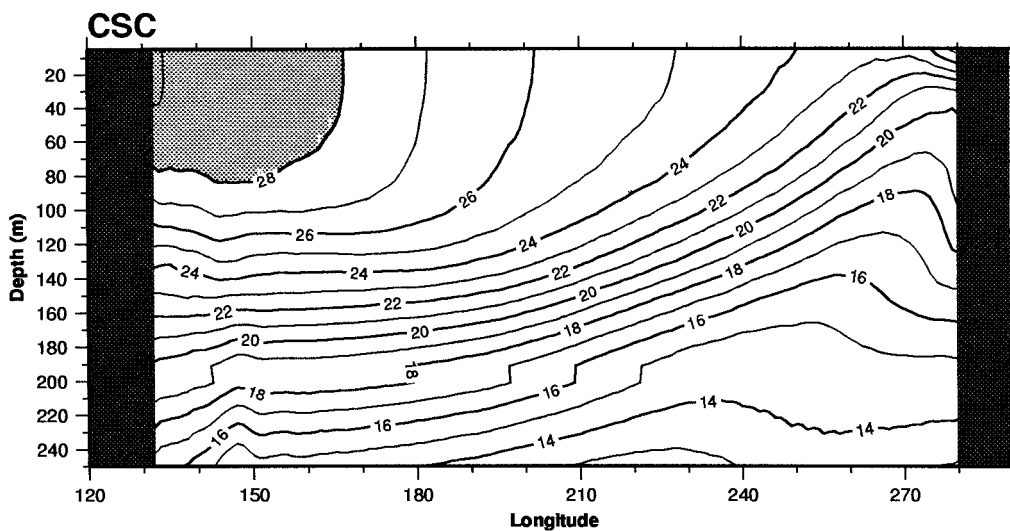
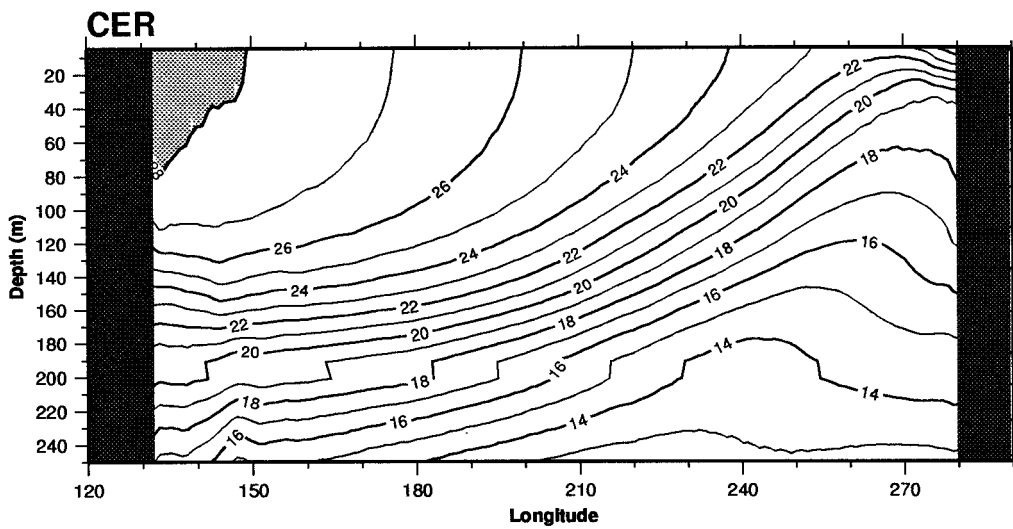
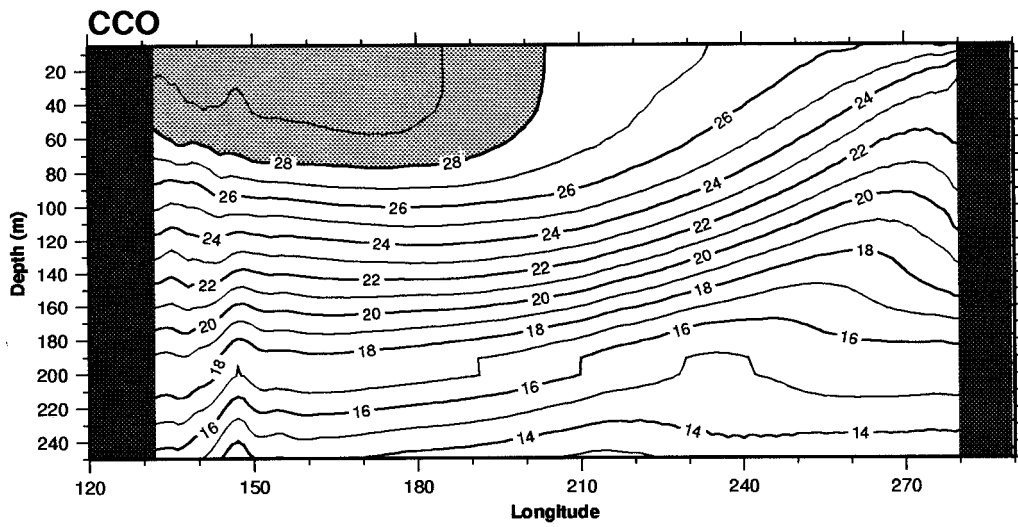
FIG. 16. Meridional ocean cross sections at 150°W of annual mean zonal current velocity U and vertical velocity W simulated with (a), (d) CCO; (b), (e) CER; and (c), (f) CSC. Panels (a), (b), (c) are zonal current velocities and (d), (e), (f) are vertical velocities. In (a), (b), (c), units are in m s^{-1} and contour intervals are every 0.2 m s^{-1} . Shading corresponds to negative values, i.e., westward currents. In (d), (e), (f), units are in m day^{-1} and contour intervals are every 0.5 m day^{-1} . Shading corresponds to values greater than 1 m day^{-1} .

the thermocline and upwelling feedbacks is crucial to determine the warm pool–cold tongue structure. The first type of feedbacks involve thermocline perturbations and are induced as a differential wave response to different wind stress fields. In this study, changes in atmospheric physical parameterizations provide the different surface wind forcing, which interacts with the ocean circulation. These processes can cause a remote response. For instance, the thermocline responds to increased easterlies in the center of the basin by shallowing to the east. This generates colder SSTs as the mixed layer is able to access colder water due to the raised thermocline. The second type of feedbacks can be called Ekman-induced equatorial upwelling. The prevailing easterly winds induce equatorial upwelling and hence

some degree of cooling. This process is enhanced with stronger easterlies. Furthermore, its spatial scale is set up by the atmosphere as the upwelling is local under the wind stress forcing. The coupled nature of both processes is clear as they can modify the zonal SST gradients, further increasing the trades especially to the west of the main cooling region.

The likelihood that both the thermocline and, to a lesser extent, the upwelling feedbacks play a more active role in CER and CSC can clearly be seen in the equatorial temperature and vertical velocity difference fields (Fig. 18). The CER difference plot shows cooling throughout the whole upper ocean from 160°W eastward due to a global upward shift of the isotherm structure linked with stronger zonal surface winds. The maximum

FIG. 17. Equatorial depth–longitude sections of annual mean temperature simulated with (a) CCO, (b) CER, and (c) CSC. Units are in Celsius and contour intervals are every $^{\circ}\text{C}$. Shading corresponds to values greater than 28°C .



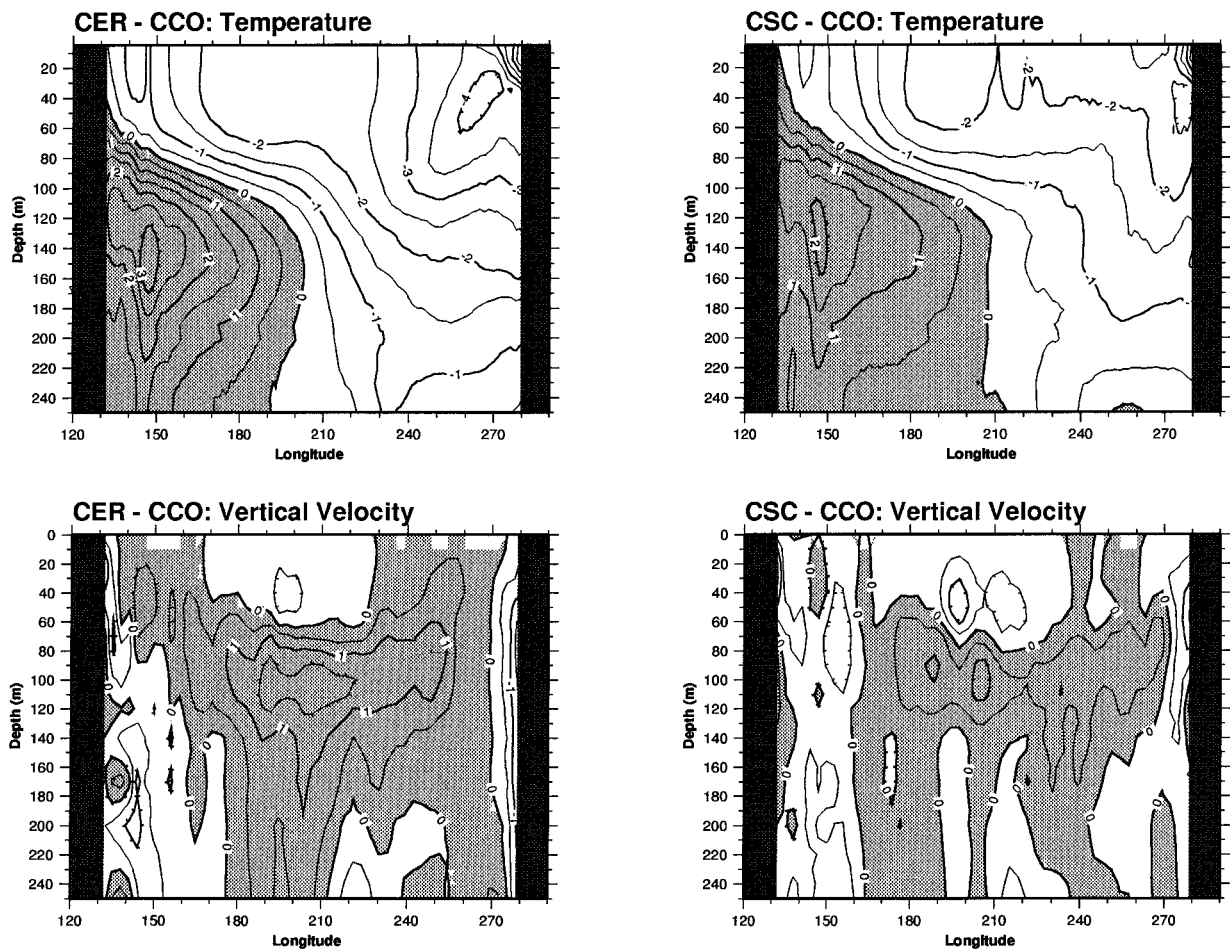


FIG. 18. Equatorial depth–longitude sections of annual mean differences in (a), (b) temperature and (c), (d) vertical velocity between CER and CCO (left panels) and CSC and CCO (right panels). In (a), (b) units are in Celsius and contour intervals are every 0.5°C . In (c), (d), units are in m day^{-1} and contour intervals are every 0.5 m day^{-1} . Shading corresponds to positive values for all panels.

temperature cooling is in the far eastern Pacific (100° – 90°W) between 20- and 60-m depths. As the mean upwelling in this region is comparable between the two simulations, the cold anomaly signal can mostly be attributed to the remote response to the steeper thermocline slope eastward of 150°W . The contribution of the thermocline feedback then decreases westward up to 130°W as shown by the strong zonal gradients in the first 100 m of the temperature difference field. The central Pacific (130°W – 170°E) region is characterized by a quasi-homogeneous cooling from the surface down to 70 m. While the equatorial upwelling is slightly weaker in CER in the first 60 m, the vertical velocity difference field exhibits large positive values between 80- and 130-m depths. Increased upwelling at these depths linked to stronger vertical mixing due to the intense easterlies in the CER experiment leads to the simulated upper-layer homogeneous cooling. Furthermore, examination of the zonal advection term in the temperature equation for the three simulations suggests it plays a dominant role in

the central Pacific cooling observed in the CER simulation (not shown).

The CSC maps display similar patterns in the central and western Pacific with reduced amplitude for the extrema. There is no clear minimum in the eastern Pacific for the temperature difference field. It is quasi-homogeneous over the first 50 m between the date line and the South American coast suggesting that the thermocline feedback is weaker in CSC than in CER.

To summarize, the amplitude of the thermocline feedback is playing an essential role in determining the climatology of the tropical Pacific in the ARPEGE–OASIS–OPA model. Furthermore, the value of the equatorial zonal wind stress around 150°W seems to be critical in getting a thermocline feedback with reasonable strength. This, in turn, is necessary to get an SST pattern with realistic zonal and meridional gradients. However, the quantitative determination of the dominant processes involved in the simulated upper-ocean cooling observed both in CER and CSC would require a detailed spatial

analysis of all the terms in the temperature equation, which is beyond the scope of this study.

5. Conclusions

In this study we investigated the sensitivity of climate drift in a tropical coupled ocean–atmosphere model to changes in carefully chosen atmospheric physical parameterizations. Specifically, the effects of SC clouds and stronger low-level convective ER upon the climatology of the tropical Pacific were simulated and analyzed through a series of uncoupled and coupled numerical experiments. As a result of this work, a number of important points can be made.

A complex coupled ocean–atmosphere GCM is able of producing a rich variety of climatologies for the tropical Pacific when changes to the atmospheric physical parameterizations are performed. For instance, the mean climate of the CGCM has been found to be extremely sensitive to the low-level enhancement of convective ER in the determination of the cloud profile. The control simulation gives an air–sea interface mean state resembling an El Niño state, whereas the modified one (CER) yields a La Niña state. In the former case, both the atmosphere and ocean have very sluggish dynamics with too symmetric patterns. In the latter case, the Walker and Hadley cells are strongly enhanced as well as the ocean zonal circulation cell.

Uncoupled atmospheric simulations show that the modified convection scheme leads to an increased moisture content at low levels. This additional moisture is then available to be carried into the tropical convergence zones through the mean meridional and zonal circulations, thereby increasing moisture convergence and convective activity. Consequently, the Hadley and Walker cells are strongly enhanced due to a dynamical feedback between cumulus convection, the large-scale flow, and moisture convergence. Furthermore the new atmospheric state does not suffer from the double ITCZ problem. The modified convective ER reduces convection locally by altering the vertical cloud profile (more environmental air entrained at low levels) toward which large-scale variables are relaxed. Although the change in convective entrainment acts equally on both sides of the equator, its interaction with the atmospheric dynamics breaks the initial symmetric pattern through the dynamical feedback described above. This change has a tremendous effect on both the circulation and thermal structure of the equatorial ocean when implemented in the coupled system. The strong zonal winds at 150°W do increase the equatorial temperature zonal tilt, which favors the thermocline feedback process. In the eastern Pacific, the mean upwelling is able to access much colder water due to the raised thermocline. The resulting cooling is then advected westward through the mean zonal circulation and leads to the cooling of the western Pacific and the associated shift of the convective activity over the Indian Ocean. Despite being on the cold side,

the SST distribution exhibits more realistic zonal gradients than the control simulation.

Implementation of a new diagnostic parameterization for SC clouds yield large changes in both SSTs and surface fluxes. As found by other authors (Ma et al. 1996), the presence of SC in the eastern basins of the subtropical oceans strongly reduces the surface solar radiation locally and yields colder SSTs in these regions. The SST distribution for the CSC experiment is actually the most realistic one, with zonal and meridional SST gradients close to the observed ones. The larger zonal thermal gradients give an increased wind stress in the east and central Pacific leading to stronger oceanic advection through the SEC. However, the double ITCZ bias is not alleviated in the CSC experiment although the SST distribution displays realistic zonal and meridional asymmetries. This confirms the atmospheric origin of the double ITCZ problem in the OPA–ARPEGE coupled model. Analysis of the PBL structure in the three simulations suggests a positive feedback between shallow and deep convection and surface evaporation, which would contribute to the maintenance of the double ITCZ in the CSC case despite realistic SSTs in the southeastern Pacific.

For coupled models to capture the dominant processes determining the climatology and variability in the tropical Pacific, it is crucial to adequately represent the spatial and temporal variations in convective activity as well as its sensitivity to sea surface temperature. Other critical processes include the realistic simulation of the thermocline and upwelling feedbacks, cloud cover and the representation of the interaction of convection with the planetary boundary layer, and its impact on surface fluxes. This last point is probably mandatory to solve both the double ITCZ and lack-of-stratus problems. Coupled modeling studies focusing on PBL physics are deeply needed as its thermodynamics modulates the surface fluxes and provides the link between the SST and the atmospheric flow.

Finally, it is anticipated that these changes in the mean climate of the tropical Pacific region could strongly modify the simulated interannual variability (Moore 1995), which is very weak in the original version [the one used for the CCO simulation; Terray et al. (1995)]. A detailed study of the seasonal cycle and El Niño–Southern Oscillation variability is under way with a 30-yr simulation of the model incorporating both effects; results will be given in a subsequent publication.

Acknowledgments. This work was supported in part by the EEC Contract ENV4-CT95-0102 SIDDACLICH. All computations were performed on the CRAY 2 at the computing center of Météo-France, Toulouse. The Vairmer package (Guilyardi 1996) based on the GMT graphic software (Wessel and Smith 1991) has been used to produce all the figures. Fruitful discussions with Henk Dijkstra and Ron Miller are gratefully acknowledged. Discussions with the participants of the Coupled GCM

Study Group meetings organized by Pascale Delecluse, Roberto Mechoso, and George Philander provided strong stimulation during the course of this work.

REFERENCES

- Blanke, B., and P. Delecluse, 1993: Low frequency variability of the tropical Atlantic Ocean simulated by a general circulation model with mixed layer physics. *J. Phys. Oceanogr.*, **23**, 1363–1388.
- Bougeault, P., 1985: A simple parameterization of the large-scale effects of deep cumulus convection. *Mon. Wea. Rev.*, **113**, 2108–2121.
- Dandin, P., 1993: Variabilité basse fréquence simulée dans l'océan pacifique tropical. Ph.D. thesis, University of Paris VI, 273 pp. [Available from Laboratoire d'Océanographie Dynamique et de Climatologie, Université Paris VI, Paris 75252, France.]
- Delecluse, P., G. Madec, M. Imbard, and C. Levy, 1993: OPA version 7 Ocean General Circulation Model reference manual. LODYC Int. Rep. 93/05, 60 pp. [Available from Laboratoire d'Océanographie Dynamique et de Climatologie, Université Paris VI, Paris 75252, France.]
- Déqué, M., C. Dreveton, A. Braun, and D. Cariolle, 1994: The climate version of Arpege/IFS: A contribution to the French community climate modelling. *Climate Dyn.*, **10**, 249–266.
- Deser, C., and J. M. Wallace, 1990: Large-scale atmospheric circulation features of warm and cold episodes in the tropical Pacific. *J. Climate*, **3**, 1254–1280.
- Dijkstra, H. A., and J. D. Neelin, 1995: Ocean–atmosphere interaction and the tropical climatology. Part II: Why the Pacific cold tongue is in the east. *J. Climate*, **8**, 1343–1359.
- ETOP5, 1986: 5' × 5' topography and elevation. Marine Geology and Geophysics Division, National Geophysical Data Center. [Available from National Geophysical Data Center, NOAA, Code E/GC3, Boulder, CO 80303.]
- Fujio, S., and N. Imasato, 1991: Diagnostic calculation for circulation and water mass movement in the deep Pacific. *J. Geophys. Res.*, **96**, 759–774.
- Geleyn, J. F., 1987: Use of a modified Richardson number for parameterizing the effect of shallow convection. *J. Meteor. Soc. Japan*, (special NWP Symp. vol.), 141–149.
- , and A. Hollingsworth, 1979: An economical analytic method for the computation of the interaction between scattering and line absorption of radiation. *Beitr. Phys. Atmos.*, **52**, 1–16.
- , and Coauthors, 1994: Atmospheric parameterization schemes in Météo-France ARPEGE NWP model. *Proc. ECMWF Workshop on Parameterization of Sub-Grid Scale Physical Processes*, Reading, United Kingdom, ECMWF, 385–402.
- Giese, B. S., and J. A. Carton, 1994: The seasonal cycle in a coupled ocean–atmosphere model. *J. Climate*, **7**, 1208–1217.
- Gregory, D., 1994: The representation of moist convection in atmospheric models. *Proc. ECMWF Workshop on Parameterization of Sub-Grid Scale Physical Processes*, Reading, United Kingdom, ECMWF, 77–113.
- , and P. R. Rowntree, 1990: A mass flux convection scheme with representation of cloud ensemble characteristics and stability dependent closure. *Mon. Wea. Rev.*, **118**, 1483–1506.
- Guilyardi, E., 1996: The VAIRMER experiment manager version 2.3. CERFACS Tech. Rep. CERFACS TR/CMGC/96-20, 102 pp. [Available from CERFACS, 42 ave. G. Coriolis, 31057 Toulouse, France.]
- Klein, S. A., and D. L. Hartmann, 1993: The seasonal cycle of low stratiform clouds. *J. Climate*, **6**, 1587–1606.
- Levitus, S., 1982: *Climatological Atlas of the World Ocean*. NOAA Prof. Paper 13, U.S. Government Printing Office, Washington, DC, 173 pp.
- Louis, J. F., M. Tiedke, J. F. Geleyn, 1982: A short history of the operational PBL parameterization at ECMWF. *Proc. ECMWF Workshop on Planetary Boundary Layer Parameterization*, Reading, United Kingdom, ECMWF, 59–80.
- Ma, C. C., C. R. Mechoso, A. Robertson, and A. Arakawa, 1996: Peruvian stratus clouds and the tropical Pacific circulation: A coupled ocean–atmosphere GCM study. *J. Climate*, **9**, 1635–1645.
- Maes, C., G. Madec, and P. Delecluse, 1997: Sensitivity of an equatorial Pacific OGCM to the lateral diffusion. *Mon. Wea. Rev.*, **125**, 958–971.
- Mechoso, C. R., and Coauthors, 1995: The seasonal cycle over the tropical Pacific in coupled ocean–atmosphere general circulation models. *Mon. Wea. Rev.*, **123**, 2825–2838.
- Meehl, G. A., 1990: Development of global coupled ocean–atmosphere general circulation models. *Climate Dyn.*, **5**, 19–33.
- , 1995: Global coupled general circulation models. *Bull. Amer. Meteor. Soc.*, **76**, 951–957.
- Mitchell, T. P., and J. M. Wallace, 1992: The annual cycle in equatorial convection and sea surface temperature. *J. Climate*, **5**, 1140–1156.
- Moore, A. M., 1995: Tropical interannual variability in a global coupled GCM: Sensitivity to mean climate state. *J. Climate*, **8**, 807–825.
- Neelin, J. D., and H. A. Dijkstra, 1995: Ocean–atmosphere interaction and the tropical climatology. Part I: The dangers of flux correction. *J. Climate*, **8**, 1325–1342.
- , and Coauthors, 1992: Tropical air–sea interaction in general circulation models. *Climate Dyn.*, **7**, 73–104.
- , M. Latif, and F. F. Jin, 1994: Dynamics of coupled ocean–atmosphere models: The tropical problem. *Annu. Rev. Fluid Mech.*, **26**, 617–659.
- Oberhuber, J. M., 1988: An atlas based on the COADS dataset: The budget of heat, buoyancy and turbulent kinetic energy at the surface of the global ocean. Max-Planck-Institut für Meteorologie Rep. No. 15, 20 pp.
- Philander, S. G. H., D. Gu, D. Halpern, G. Lambert, N. C. Lau, T. Li, and R. C. Pacanowski, 1996: The role of low-level stratus clouds in keeping the ITCZ mostly north of the equator. *J. Climate*, **9**, 2958–2972.
- Randall, D. A., 1994: The role of clouds in the general circulation of the atmosphere. *Proc. ECMWF Workshop on Parameterization of Sub-Grid Scale Physical Processes*, Reading, United Kingdom, ECMWF, 33–42.
- Reynolds, R. W., 1988: A real-time global sea surface temperature analysis. *J. Climate*, **1**, 75–86.
- Ritter, B., and J. F. Geleyn, 1992: A comprehensive radiation scheme for numerical weather prediction models with potential applications in climate simulations. *Mon. Wea. Rev.*, **120**, 303–325.
- Rossow, W. B., and R. A. Schiffer, 1991: ISCCP cloud data products. *Bull. Amer. Meteor. Soc.*, **72**, 2–20.
- Sarmiento, J. L., and K. Bryan, 1982: An ocean transport model for the North Atlantic. *J. Geophys. Res.*, **87**, 394–408.
- Simpson, J., 1971: On cumulus entrainment and one-dimensional models. *J. Atmos. Sci.*, **28**, 449–455.
- Slingo, J. M., 1987: The development and verification of a cloud prediction scheme for the ECMWF model. *Quart. J. Roy. Meteor. Soc.*, **113**, 899–927.
- Terray, L., 1995: The OASIS Coupler User Guide Version 2.0. CERFACS Tech. Rep. CERFACS TR/CMGC/95-46, 100 pp. [Available from CERFACS, 42 ave. G. Coriolis, 31057 Toulouse, France.]
- , O. Thual, S. Belamari, M. Déqué, P. Dandin, P. Delecluse, and C. Lévy, 1995: Climatology and interannual variability simulated by the ARPEGE-OPA coupled model. *Climate Dyn.*, **11**, 487–505.
- Wessel, P., and W. H. F. Smith, 1991: Free software helps map and display data. *Eos, Trans. Amer. Geophys. Union*, **72**, 441, 445–446.
- Xie, S. P., 1994: The maintenance of an equatorially asymmetric state in a hybrid coupled GCM. *J. Atmos. Sci.*, **51**, 2602–2612.
- , and S. G. H. Philander, 1994: A coupled ocean–atmosphere model of relevance to the ITCZ in the eastern Pacific. *Tellus*, **46A**, 340–350.